Dalton Transactions

ROYAL SOCIETY OF CHEMISTRY

PAPER

Check for updates

Cite this: *Dalton Trans.*, 2020, **49**, 8247

Solid-state to solution helicity inversion of pseudotetrahedral chiral copper(II) complexes with 2,4-dihalo-salicylaldiminate ligands†

Nazanin Kordestani,[a] Hadi Amiri Rudbari, *[a] Giuseppe Bruno, [b] Scopelliti Rosario,[c] Jason D. Braun, [d] David E. Herbert, [d] Olivier Blacque, [e] Isabel Correia, [f] Mohammad Al-moktadir Zaman,[g] Mortuza Mamun Bindu,[g] Christoph Janiak *[h] and Mohammed Enamullah *[g]

The enantiopure Schiff bases (*R* or *S*)-*N*-1-(phenyl)ethyl-2,4-X^1,X^2-salicylaldimine (X^1, X^2 = Cl, Br, I) coordinate to copper(II) and provide pseudotetrahedral bis[(*S* or *R*)-*N*-1-(phenyl)ethyl-(2,4-X^1,X^2-salicylaldiminato-κ^2N,O)]-Δ/Λ-Cu(II) (Λ/Δ-Cu-*R* or Δ/Λ-Cu-*S*). An induced Λ and Δ-chirality at-metal centre has been launched along the C_2-axis of the molecule. Steric constraints brought by halogen substituents on the coordinating salicylal ring provide diastereoselectively Λ-Cu-*R* or Δ-Cu-*S* as major and Δ-Cu-*R* or Λ-Cu-*S* as minor diastereomers at solid-state, as evidenced by X-ray crystal structures and PXRD analyses. These results reveal inversion of induced chirality at-metal in comparison to the similar complexes without halogen substituents on the salicylal ring. Electronic circular dichroism (ECD) spectra show mirror-image relationships, confirming enantiomeric excess of the *R* or *S*-ligated complexes in solution. Comparisons of experimental and simulated ECD spectra suggest diastereomeric excess of Δ-Cu-*R* or Λ-Cu-*S* in solution which correspond to an inversion from the found solid-state Λ-Cu-*R* or Δ-Cu-*S* as major diastereomers. In addition, the optimized gas-phase structures also reveal Δ-Cu-*R* or Λ-Cu-*S* as slightly more stable than Λ-Cu-*R* or Δ-Cu-*S*. Thus, solid-state *versus* solution (or gas-phase) studies also indicate an interconversion of induced chirality (helicity inversion) at-metal from Λ-Cu-*R* or Δ-Cu-*S* to Δ-Cu-*R* or Λ-Cu-*S*. Thermal stability increases with the molecular weight of the complexes following Cl < ClBr < Br < I substituents. Hirshfeld surface analyses explore the strongest halogen (*ortho*)–halogen (*para*) interactions between two molecules in Λ-Cu-*R*3 or Δ-Cu-*S*3 at a distance shorter than the sum of the van der Waals radii of the two iodine atoms, provide a brilliant red spot on the d_{norm} surfaces. EPR spectra along with simulation suggest an axial symmetry with $g_z > g_{x,y} > 2.0$ and values for $g_z/A_z \geq 135$ cm indicate pseudotetrahedral geometry for the complexes.

Received 6th May 2020,
Accepted 2nd June 2020

DOI: 10.1039/d0dt01649g

rsc.li/dalton

[a]*Department of Chemistry, University of Isfahan, Isfahan 81746-73441, Iran. E-mail: h.a.rudbari@sci.ui.ac.ir*
[b]*Department of Chemical, Biological, Pharmaceutical and Environmental Sciences, University of Messina, Viale Ferdinando Stagno D'Alcontres 31, I-98166 Messina, Italy*
[c]*Institut des Sciences et Ingénierie Chimiques, École Polytechnique Fédérale de Lausanne (EPFL), CH-1015 Lausanne, Switzerland*
[d]*Department of Chemistry, University of Manitoba, Winnipeg, Manitoba R3T 2N2, Canada*
[e]*Department of Chemistry, University of Zurich, Winterthurerstrasse 190, CH-8057 Zurich, Switzerland*
[f]*Centro de Química Estrutural, Departamento de Engenharia Química, Instituto Superior Técnico, Universidade de Lisboa, Av Rovisco Pais, 1049-001 Lisboa, Portugal*
[g]*Department of Chemistry, Jahangirnagar University, Dhaka 1342, Bangladesh. E-mail: enamullah@juniv.edu*
[h]*Institut für Anorganische Chemie und Strukturchemie, Universität Düsseldorf, D-40204 Düsseldorf, Germany*

†Electronic supplementary information (ESI) available: Optimized structures, simulated UV-Vis./CD spectra, Hirshfeld surfaces, EPR/PXRD data, CIF/CHECKCIF files and excited state properties. CCDC 1943411–1943414, 1943417–1943420 and 1964878. For ESI and crystallographic data in CIF or other electronic format see DOI: 10.1039/d0dt01649g

Introduction

Transition metal-complexes with enantiopure (*S* or *R*)-N,O-chelate Schiff base ligands have attracted considerable interest in the context of diastereoselection and induced chirality at-metal center[1–5] and as potential *chiral*-catalysts for stereoselective syntheses.[6,7] If two bidentate N,O-chelate ligands (N^O) coordinate in a non-planar mode in a four-coordinated $M(N^O)_2$ complex then chirality at-metal is introduced in a C_2-symmetric complex with the opposite configured stereoisomers Λ- and Δ-$M(N^O)_2$. The use of *chiral* N,O-chelate Schiff base ligands (*R* or *S*-N^O) will then give the diastereomers Λ-M(*R*-N^O)$_2$ and Δ-M(*R*-N^O)$_2$ {or Δ-M(*S*-N^O)$_2$ and Λ-M(*S*-N^O)$_2$}. Non-covalent interactions acting within the metal–ligand framework and between complexes in the solid state or between complexes and solvent molecules in the solution state lead to a free energy difference between the two diastereomers

for the enantiopure chelate ligand and hence one of the diastereomers can be favored. The favored diastereomer does not need to be the same in the solution and in the solid state. This situation arises when the Λ- and Δ-M(N^O)$_2$ stereoisomers can interconvert, *e.g.*, through a planar transition state.

We have studied the Λ-Δ-solid-state to solution helicity inversion using cobalt(II), copper(II) and zinc(II) complexes with (*R* or *S*)-N,O chelate Schiff bases, employing X-ray crystallography, thermal analyses, time and temperature dependent ^{1}H-NMR, electronic and vibrational circular dichroism (ECD/VCD) spectroscopy both in solution and at solid-state, respectively.[8–12] Comparisons of experimental and simulated ECD/VCD spectra allow to assign the absolute configuration of the metal ion in solution. Our previous results and related literatures reveal that induced metal centered chirality, in general, provides preferential formation of Λ-M-*R* or Δ-M-*S* (major diastereomers) in the most enantiopure crystals of metal(II)-(*R* or *S*)-N,O chelates.[2a,c,4c,5c,d,8,9,12,13]

It has been noted that the diastereoselection and induced chirality (Λ *vs.* Δ) arise quantitatively in the solid-state, while a dynamic diastereomeric equilibrium between the two diastereomers prevails in solution.[8–10,14] Solution ^{1}H NMR, VCD and ECD spectra show an equilibrium shifting from the only and typical diastereomer Λ-M-*R*-N,O or Δ-M-*S*-N,O in the solid-state to the diastereomer Δ-M-*R*-N,O or Λ-M-*S*-N,O upon dissolution (M = Co,[8] Zn[12]) with predominance of the latter in solutions of M = Co.

Helicity inversion can also be induced by a solvent difference as was the case from Δ- (in acetonitrile) to Λ-diastereomer (in dmso) for a *chiral* tris (diphenylethylenediamine)nickel(II) complex.[15] Epimerization of metal centered chirality in Ti(IV) and Re(I) complexes was induced by pH of the solution or solvent polarity changes.[16] Redox-driven (electron-induced) helicity inversion at-metal was reported for chiral-at-metal Co/Cu(II) complexes.[17]

The ligand substituents, inter-/intra-molecular interactions, metal ion selection, ligand folding behavior, pH, solvent, redox state, solute-solvent interactions, crystallization protocol, time and temperature can influence the induced metal centered chirality and Λ-M *vs.* Δ-M configuration or diastereomer selection (for chiral ligands) in the solid and solution state.[8–13,15–18]

The present endeavour reports results of syntheses, chiroptical properties, diastereoselection and induced metal centered chirality in pseudotetrahedral copper(II) complexes with 2,4-dihalo-salicylaldiminate ligands, bis[(*S* or *R*)-*N*-1-(phenyl)ethyl-(2,4-X^1,X^2-salicylaldiminato-κ^{2}N,O)]-Δ/Λ-Cu(II) (Scheme 1). The halogen substituents on the salicylal-ring were incorporated in view of fine tuning the phenomenon in the context of steric constraints and solid-state *versus* solution studies.

Results and discussion

The enantiopure (*S* or *R*)-N,O-chelate Schiff bases, (*S* or *R*)-*N*-1-(phenyl)ethyl-2,4-X^1,X^2-salicylaldimine (X^1 = X^2 = Cl (*R* or *S*-H1); Br (*R* or *S*-H2); I (*R* or *S*-H3); X^1, X^2 = Br, Cl (*R* or *S*-H4)) were synthesized by condensation of the 2-hydroxy-3,5-dihalogen salicylaldehyde with the enantiopure amine (*R* or *S*)-α-methyl-benzylamine, respectively (Scheme 1). The ^{1}H-NMR spectra show a singlet at δ 8.15–8.30 ppm for the imine proton (C*H*N), while a broad signal resonating at δ 14.73–15.01 ppm is assigned to the O*H* group. A quartet is found at *ca.* δ 4.70 ppm for the methine proton (C*H*) and a doublet at *ca.* δ 1.70 ppm for the methyl group. The ^{1}H-/^{13}C-NMR spectral data are listed in the Experimental section, and agree well with data reported in the literature.[19] Syntheses of the copper(II) complexes, bis[(*S* or *R*)-*N*-1-(phenyl)ethyl-(2,4-X^1,X^2-salicylaldiminato-κ^{2}N,O)]-Δ/Λ-Cu(II) {X^1 = X^2 = Cl (Cu-*R*1 or Cu-*S*1); Br (Cu-*R*2 or Cu-*S*2); I (Cu-*R*3 or Cu-*S*3) and X^1, X^2 = Br, Cl (Cu-*R*4 or Cu-*S*4)} were carried out using a common procedure as mentioned in Experimental section.[9] The reaction yields mononuclear species where the metal ion is surrounded by two N,O-chelate ligands with pseudotetrahedral geometry (Scheme 1). The IR spectra exhibit a common characteristic band for the Schiff bases at 1625–1628 cm^{-1} for ν(C=N),[19] which shifts to lower wavenumbers at 1600–1608 cm^{-1} upon coordination to the metal ion.[8–12] The very low values of molar conductance (Λ_m = 0.55–1.80 S cm^2 mol^{-1} in DMF) correspond to the non-electrolyte behavior of the complexes with metal to ligand 1 : 2 stoichiometry ([ML$_2$]) in solution.[20]

X-ray structure analyses

The X-ray molecular structures for the bis[(*S* or *R*)-*N*-1-(phenyl)ethyl-(2,4-X^1,X^2-salicylaldiminato-κ^{2}N,O)]-Δ/Λ-Cu(II) {X^1 = X^2 = Cl (Cu-*R*1 or Cu-*S*1); Br (Cu-*R*2 or Cu-*S*2); I (Cu-*R*3 or Cu-*S*3) and X^1/X^2 = Br/Cl (Cu-*R*4 or Cu-*S*4)} are shown in Fig. 1. Some selected bond lengths and angles are listed in Tables 1 and 2. The structural data are comparable to the analogous copper(II) complexes with (*S* or *R*)-*N*-1-(*p*-X-Ar)ethyl-salicylaldiminate.[11] The complexes crystallize in non-centrosymmetric space groups C_2 for Λ-Cu-*R*1, Λ-Cu-*R*2, Λ-Cu-*R*3, Δ-Cu-*S*3 and Λ-Cu-*R*4; I_2 for Δ-Cu-*S*2 and Δ-Cu-*S*4 and $P2_1$ for Λ-Cu-*S*1 (#1 and #2). The molecular structure determination demonstrates that the metal ion is four-coordinated by two phenolate-oxygen and two imine-nitrogen atoms from the two Schiff base ligands in pseudotetrahedral geometry. The asymmetric unit for all complexes contains half of the molecule that lies on a crystallographic 2-fold axis passing through the copper atom except Λ-Cu-*S*1 (#1 and #2) which contains a full molecule (Fig. 1). Examination of metal–ligand distances reveals that the Cu–O bond is shorter than Cu–N due to strong bonding between the negatively charged oxygen atom (O$^-$) and the positively charged copper(II) ion (Tables 1 and 2).

By considering the C_2-axis (in Λ-Cu-*R*1, Λ-Cu-*R*2/Δ-Cu-*S*2, Λ-Cu-*R*3/Δ-Cu-*S*3 and Λ-Cu-*R*4/Δ-Cu-*S*4) or pseudo C_2-axis (in Λ-Cu-*S*1) passing through the center of O1···O1′ edge (O1···O2 in Λ-Cu-*S*1), metal atom and center of N1···N1′ edge (N1···N2 in Λ-Cu-*S*1), the absolute configuration of Δ or Λ-form is determined (Scheme 1) and denoted as part of complexes' designation. For a given *S* or *R*-ligand chirality, only one Δ or Λ-configuration is found in each investigated crystal on the basis of

 This journal is © The Royal Society of Chemistry 2020

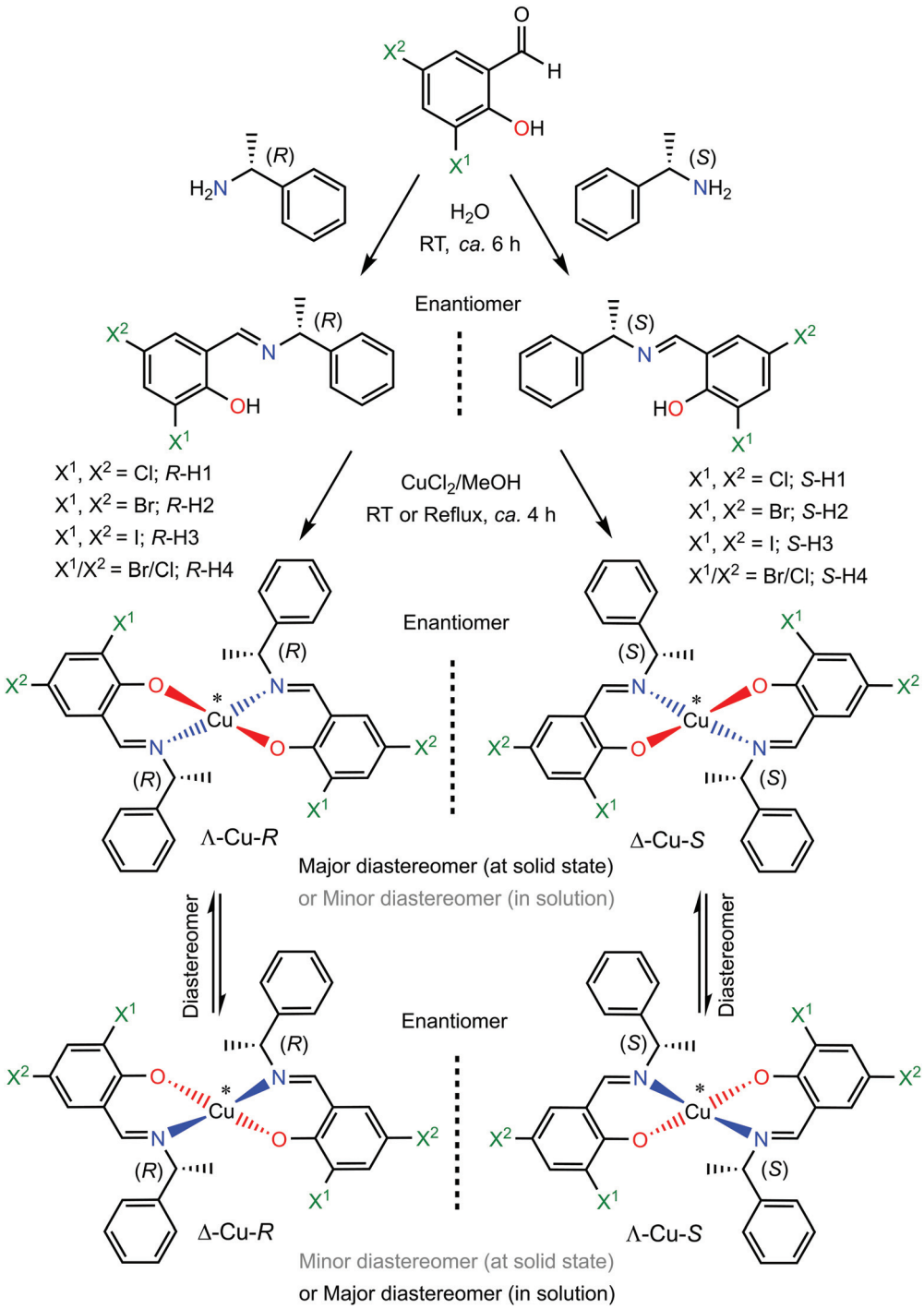

Scheme 1 Synthetic route to the formation of enantiopure (*R* or S)-N,O chelate Schiff bases and bis[(*S* or *R*)-*N*-1-(phenyl)ethyl-(2,4-X^1,X^2-salicylaldiminato-κ^2N,O)]-Δ/Λ-Cu(II) complexes.

absolute structure or Flack parameter values for −0.03 to +0.06 (Tables 9 and 10).[8–13,21]

Indeed, Flack parameter values close to zero and other refinement parameters (*e.g.*, normal atom temperature factors and absence of any molecular disorder) rule out any significant amount of molecule with opposite chirality at-metal centre. This means that there is no diastereomeric mixture (*i.e.*, both Δ-Cu and Λ-Cu) within one of the investigated enantiopure crystals. The Δ-Cu or Λ-Cu configuration is induced diastereospecifically by the conformational preference of the N,O-chelate rings, resulting from steric requirements of the substituents groups and/or chirality of the ligands. The more general preference for observed Λ-Cu-*R* or Δ-Cu-*S* configuration (as major diastereomer at solid-state) is thought to be

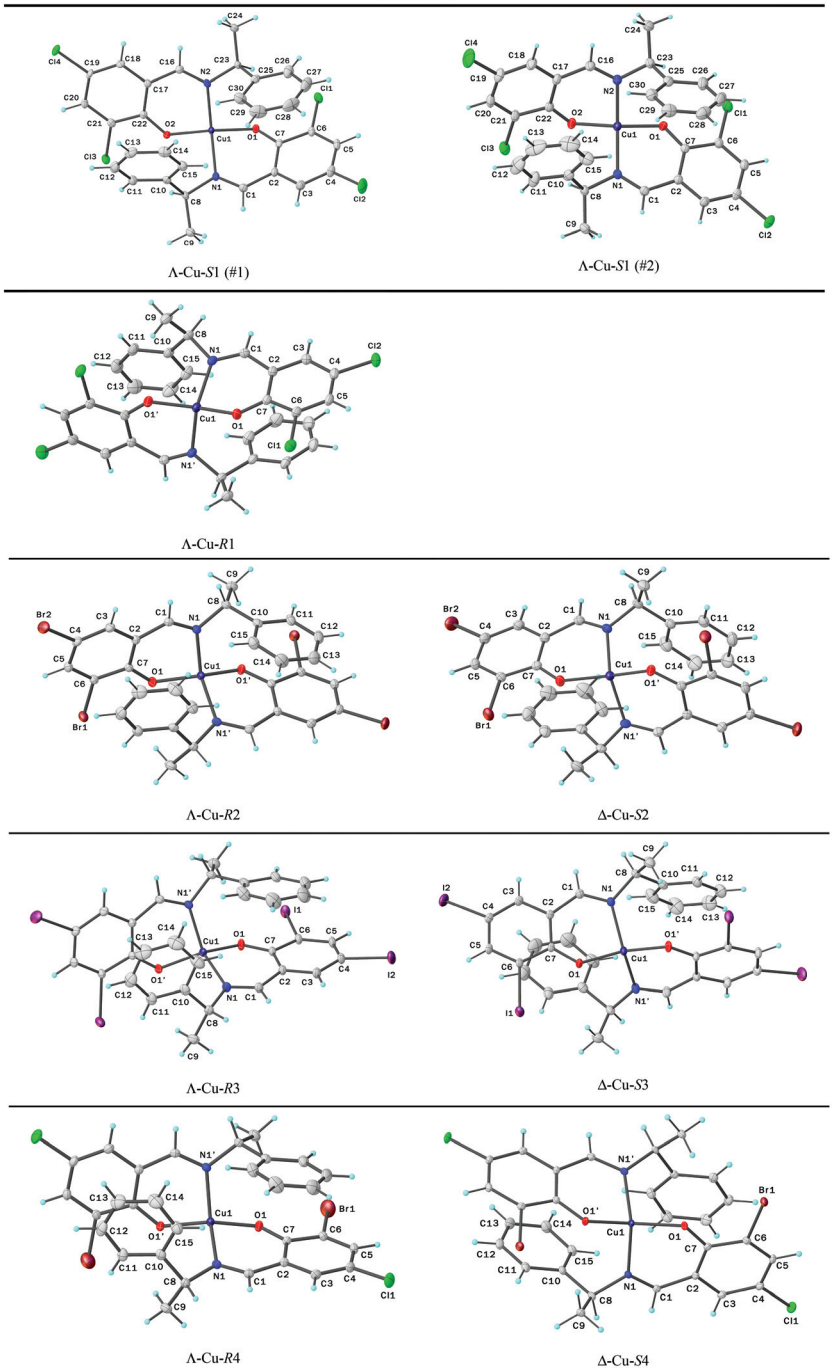

Fig. 1 Molecular structures for the enantiopure complexes with Λ-Cu-*R* and Δ-Cu-*S* configurations in pseudotetrahedral N_2O_2-coordination sphere (see Tables 1, 2 for bond lengths and angles).

driven by minimization of steric constraints (leading to thermodynamic stability) by the chelating rings in the coordination sphere. These results are in parallel to the more common findings of preferred formation of Λ-M-*R* or Δ-M-*S* as major diastereomer in the transition metal(II) complexes with (*S* or *R*)-*N*-1-(*p*-X-Ar)ethyl-salicylaldiminate/-oxo-naphthaldiminate (X = H, OCH_3, Cl, Br) at solid-state.[8–10,12,13,18] However, opposite findings of induced chirality with preferred formation of Δ-M-*R* or Λ-M-*S* were reported in the analogous copper(II)-(*p*-X-Ar)ethyl-salicylaldiminate.[11] The only difference between the presently investigated complexes and the later complexes is the halogen substituents on the salicylal-ring. These results strongly support the notion that the steric constraints brought by the halogen substituents on the coordinating salicylal-ring lead to helicity inversion of the copper centre and thereby, control the metal centered chirality (Δ *vs.* Λ).

 This journal is © The Royal Society of Chemistry 2020

Table 1 Selected bond lengths (Å) and angles (°) for the compounds

Entity	Λ-Cu-*R*1	Λ-Cu-*R*2	Λ-Cu-*R*3	Λ-Cu-*R*4	Δ-Cu-*S*2	Δ-Cu-*S*3	Δ-Cu-*S*4
Cu1–O1/O1′	1.883(3)	1.8819(19)	1.885(2)	1.882(2)	1.879(2)	1.885(4)	1.889(3)
Cu1–N1/N1′	2.012(4)	2.013(2)	2.018(2)	2.016(2)	2.020(2)	2.012(4)	2.012(3)
C(1)–N1	1.285(6)	1.286(4)	1.288(4)	1.275(4)	1.269(4)	1.292(7)	1.282(5)
O1–Cu1–O1′	143.0(2)	143.69(12)	143.18(15)	143.53(13)	143.08(14)	143.1(3)	144.06(18)
N1–Cu1–N1′	131.3(2)	130.12(12)	129.86(16)	131.96(14)	130.20(14)	129.7(3)	131.71(19)
O1–Cu1–N1′	102.17(15)	101.77(9)	101.92(10)	101.75(9)	102.18(10)	101.86(18)	101.68(12)
O1–Cu1–N1	92.90(14)	93.37(9)	93.50(9)	92.93(9)	93.19(10)	93.63(17)	92.86(12)

Symmetry transformations used to generate equivalent atoms: $-x+1, y, -z$ for Λ-Cu-*R*1; $-x+1, y, -z+1$ for Λ-Cu-*R*2; $-x+1, y, -z+1$ for Λ-Cu-*R*3; $-x+1, y, -z+1$ for Λ-Cu-*R*4; $-x+1, y, -z+1$ for Δ-Cu-*S*2; $-x+1, y, -z+1$ for Δ-Cu-*S*3; $-x+1, y, -z+1$ for Δ-Cu-*S*4.

Table 2 Selected bond lengths (Å) and angles (°) for Λ-Cu-S1[a]

Entity	Λ-Cu-*S*1 (#1)	Λ-Cu-*S*1 (#2)	Entity	Λ-Cu-*S*1 (#1)	Λ-Cu-*S*1 (#2)
Cu1–O1	1.8988(18)	1.8785(14)	O1–Cu1–O2	151.36(8)	150.92(7)
Cu1–O2	1.8814(17)	1.8924(15)	N1–Cu1–N2	145.61(9)	144.70(8)
Cu(1)–N1	2.001(2)	1.9807(17)	O1–Cu1–N1	91.94(8)	93.65(7)
Cu1–N2	1.985(2)	1.9970(19)	O2–Cu1–N1	94.29(8)	97.28(7)
C1–N1	1.280(4)	1.285(3)	O1–Cu1–N2	96.93(8)	94.55(7)
C16–N2	1.286(3)	1.285(3)	O2–Cu1–N2	93.57(8)	91.95(7)

[a] From two separate crystals (#1 and #2).

Based on literature[8–10,12,13,18] and present investigation, in general, the *S* or *R*-ligand chirality along with the steric constraints always provide the opposite configured Δ-Cu-*S* or Λ-Cu-*R* as major diastereomer and Λ-Cu-*S* or Δ-Cu-*R* as minor diastereomer and *vice versa* (Scheme 1) at solid-state. In contrary to these findings, the chloro-substituted complexes with *S*-ligand show the minor diastereomer Λ-Cu-*S*1 (#1) instead of major diastereomer Δ-Cu-*S*1. To check this anomaly, we repeated the measurement with a new set of Cu-*S*1 crystals and found similar results as of Λ-Cu-*S*1 (#2) (Fig. 1 and Table 2). It could happen that for both data sets (#1 and #2), a single crystal of minor diastereomer (Λ-Cu-*S*1) was selected by chance (see further details in PXRD analyses).

Quantitative analyses of pseudotetrahedral geometry

The solid-state structures (Fig. 1) show that the geometry for four-coordinated bis(N,O-chelate)-copper(II) complexes deviates substantially from tetrahedral to pseudotetrahedral. This distortion can be calculated quantitatively by the dihedral angle (θ/°) between the two chelates planes N1–Cu–O1 and N1′–Cu–O1′.[8–12] The θ values are 90° for tetrahedral and 0° for square-planar geometry (not considering the distortion induced by the chelate ring formation). In addition, two geometric indexes $\tau_{\text{tet-sq}}$ [22] and τ_4 [23] have successfully been used to determine quantitatively this distortion, whose values are 1.0 for tetrahedral and 0 for square-planar geometry. The observed values for θ (60–62°), $\tau_{\text{tet-sq}}$ (0.67–0.68) and τ_4 (0.60–0.62) are almost the same along the series, except for Λ-Cu-*S*1 (θ = 44.2° (#1) and 45.2° (#2)) (Table 3). Further, these values are very close to the corresponding calculated values from the optimized structures (Table 3). These results strongly suggest the pseudotetrahedral geometry for all investigated complexes.

Table 3 Measurements of dihedral angle (θ/°) and geometric indexes ($\tau_{\text{tet-sq}}$ and τ_4)[22,23]

Compounds	θ/°[a]	$\tau_{\text{tet-sq}}$[b]	τ_4[c]
Λ-Cu-*R*1	61.04 (59.85)	0.68 (0.67)	0.61
Λ-Cu-*S*1 (#1)	44.21 (43.73)	0.49 (0.49)	0.45
Λ-Cu-*S*1 (#2)	45.18	0.50	0.46
Λ-Cu-*R*2	61.16 (60.14)	0.68 (0.67)	0.61
Δ-Cu-*S*2	61.70 (60.63)	0.67 (0.67)	0.61
Λ-Cu-*R*3	61.81	0.69	0.62
Δ-Cu-*S*3	61.96	0.69	0.62
Λ-Cu-*R*4	60.14 (59.06)	0.67 (0.66)	0.60
Δ-Cu-*S*4	60.10 (58.98)	0.68 (0.66)	0.60

[a] Values in parentheses are calculated from the optimized structures at B3LYP/6-31G(d). [b] $\tau_{\text{tet-sq}} = (\theta/90)°$. [c] $\tau_4 = [\{360° - (\alpha + \beta)\}/141]°$, where α, β are the two largest angles in four-coordinated species (see Tables 1 and 2).

Hirshfeld surface analyses (discussed below) show that the contributions for Cl···Cl, Cl···H, Cl···C and C···H intermolecular contacts are relatively less (*i.e.*, weaker contacts) in Λ-Cu-*S*1 (#1 and #2) in comparison to those found in Λ-Cu-*R*1, which provide the former one with relatively low values for θ (44–45°) and $\tau_{\text{tet-sq}}/\tau_4$ (0.49–0.50/0.45–0.46). As a result, relatively less distortion from the normally for Cu(II) expected square-planar to tetrahedral geometry is found for Λ-Cu-*S*1, *i.e.*, the geometry is half-way in between tetrahedral and square-planar and not distorted more towards tetrahedral as the other compounds (Table 3).

PXRD analyses

Experimental PXRD patterns for the both bulk samples Cu-*S*1 and Cu-*R*1 consist of an identical crystal phase (Fig. S1, ESI†).

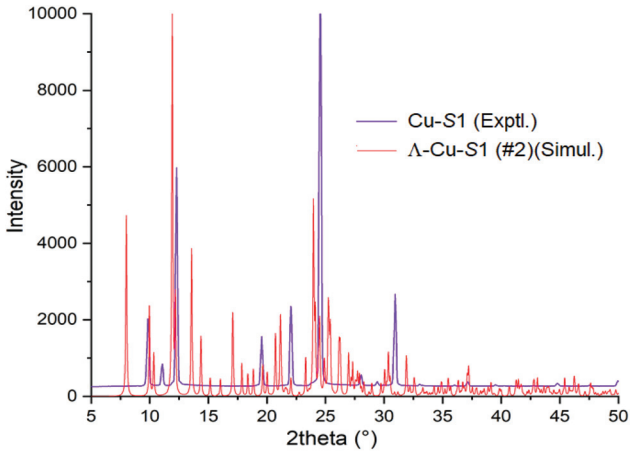

Fig. 2 Experimental PXRD from the bulk phase of Cu-*S*1 crystals and simulated PXRD from the single crystal of Λ-Cu-*S*1 (#2).

The PXRD pattern from the single crystal of Λ-Cu-*S*1 (data set #1 or #2), taken from bulk samples of Cu-*S*1, is not representative of the bulk crystal phase of Cu-*S*1 (Fig. 2). Instead the single crystal of Λ-Cu-*S*1 represents a very minor impurity whose contribution is not seen in the experimental PXRD of the bulk phase. At the same time, the PXRD from the single crystal of Λ-Cu-*R*1 is rather representative of the bulk crystal phase of Cu-*R*1 (Fig. 3). Consequently, also the bulk crystal phase of Cu-*S*1 matches relatively well to the PXRD from the single crystal of Λ-Cu-*R*1 (Fig. S2, ESI†). From comparison of Fig. 3 and Fig. S2 (ESI†) this is as expected as both experimental PXRDs of Cu-*S*1 and Cu-*R*1 match very well (*cf.* Fig. S1, ESI†).

Further, the two crystals Λ-Cu-*S*1 (#1 or #2) and Λ-Cu-*R*1 have different space groups ($P2_1$ and $C2$) which manifest themselves in significant differences in the PXRDs (Fig. S3, ESI†). As suggested before, Λ-Cu-*S*1 is indeed the minor diastereomer and single crystal of this minor-form was selected

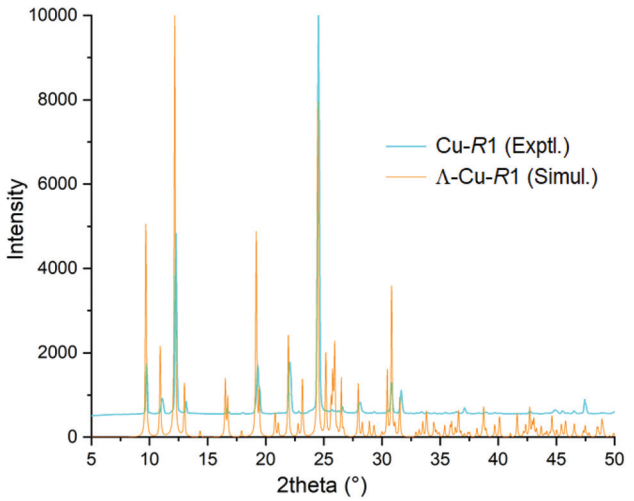

Fig. 3 Experimental PXRD from the bulk phase of Cu-*R*1 crystals and simulated PXRD from the single crystal of Λ-Cu-*R*1.

for both data sets (#1 and #2) by chance. The major diastereomer in the bulk sample of Cu-*S*1 is obviously Δ-Cu-*S*1 and hence, PXRD for this bulk sample does not match to the single crystal of Λ-Cu-*S*1 (minor diastereomer) (Fig. 2). These results suggest there are two diastereomers of Λ-Cu-*R*1 or Δ-Cu-*S*1 (major diastereomer) and Δ-Cu-*R*1 or Λ-Cu-*S*1 (minor diastereomer) in the bulk crystals sample of Cu-*R*1 or Cu-*S*1.

We would like to make it very clear, however, that the (simulated) phase Λ-Cu-*S*1 is not seen at all in the PXRD of the experimental Cu-*S*1 phase (Fig. 2), which matches only to the (unknown) Δ-Cu-*S*1 = (known) Λ-Cu-*R*1 phase (Fig. S2, ESI†). Likewise, in the experimental PXRD of Λ-Cu-*R*1 there is no evidence of a phase for (unkown) Δ-Cu-*R*1 which would have to be isostructural to Λ-Cu-*S*1 (Fig. S3, ESI†). Thus, the minor diastereomer in the solid state (Scheme 1) is not present in amounts which are detected by PXRD. Consequently, a Rietveld analysis, which would allow to quantify the ratio of the two diastereomers in the solid state, is not possible.

Hirshfeld surface analyses

The intermolecular contacts in the crystal packing of the complexes are quantified *via* the Hirshfeld surface analyses using the CrystalExplorer.[24] The Hirshfeld surfaces with d_{norm} properties and their fingerprint plots are illustrated in Fig. 4. The percentages of contributions to various types of contacts in the fingerprint plots are summarized in Fig. S4, ESI.† The plots indicate that the highest contributions over the Hirshfeld surface are due to H···H contacts (*ca.* 32%) as the molecular surface is comprised of a sea of H-atoms (Fig. 4 and S4, ESI†). As shown in Fig. 4, the H···H contacts appear as the largest area of the plots with a high concentration in the middle region (shown in light blue color). The shortest H···H interactions in the plots are presented as spikes at $d_e + d_i \sim 2.2$ Å. The large number of H-atoms over the surface also provide the highest contributions to Cl···H, Br···H, I···H and C···H contacts (*i.e.*, halogen-bond), almost same as for H···H contacts (Fig. 4 and S4, ESI†).

Surprisingly, the decomposition of the fingerprint plots indicates that iodine, bromide and chlorine intermolecular contacts cover nearly 40% of the whole Hirshfeld surface in all complexes (Fig. S4, ESI†). This can be attributed to the relatively large van der Waals radii of the halogen atoms. The decomposition of the plots for Λ-Cu-*R*4 and Δ-Cu-*S*4 indicates that Cl···H (17.2%) intermolecular contact has a higher percentage than Br···H (15.1%) on the Hirshfeld surface (Fig. S4, ESI†). But interestingly, Br···H contact distance is significantly shorter than the corresponding sum of the van der Waals radii, indicating its prominent role in crystal packing, which results in a faint red spot on the d_{norm} surface (Fig. 4). The halogen atoms undergo three kinds of non-covalent interactions including halogen bonds, halogen–halogen and halogen–π interactions (Scheme S1, ESI†).[25] The previous research showed the strongest halogen–halogen interactions for the most easily polarizable halogen atoms (*i.e.*, by iodine).[26] Thus, Λ-Cu-*R*3 and Δ-Cu-*S*3, having iodine atoms, exhibit the strongest halogen–halogen interactions with distances shorter than those of the sum of van der Waals radii in

 This journal is © The Royal Society of Chemistry 2020

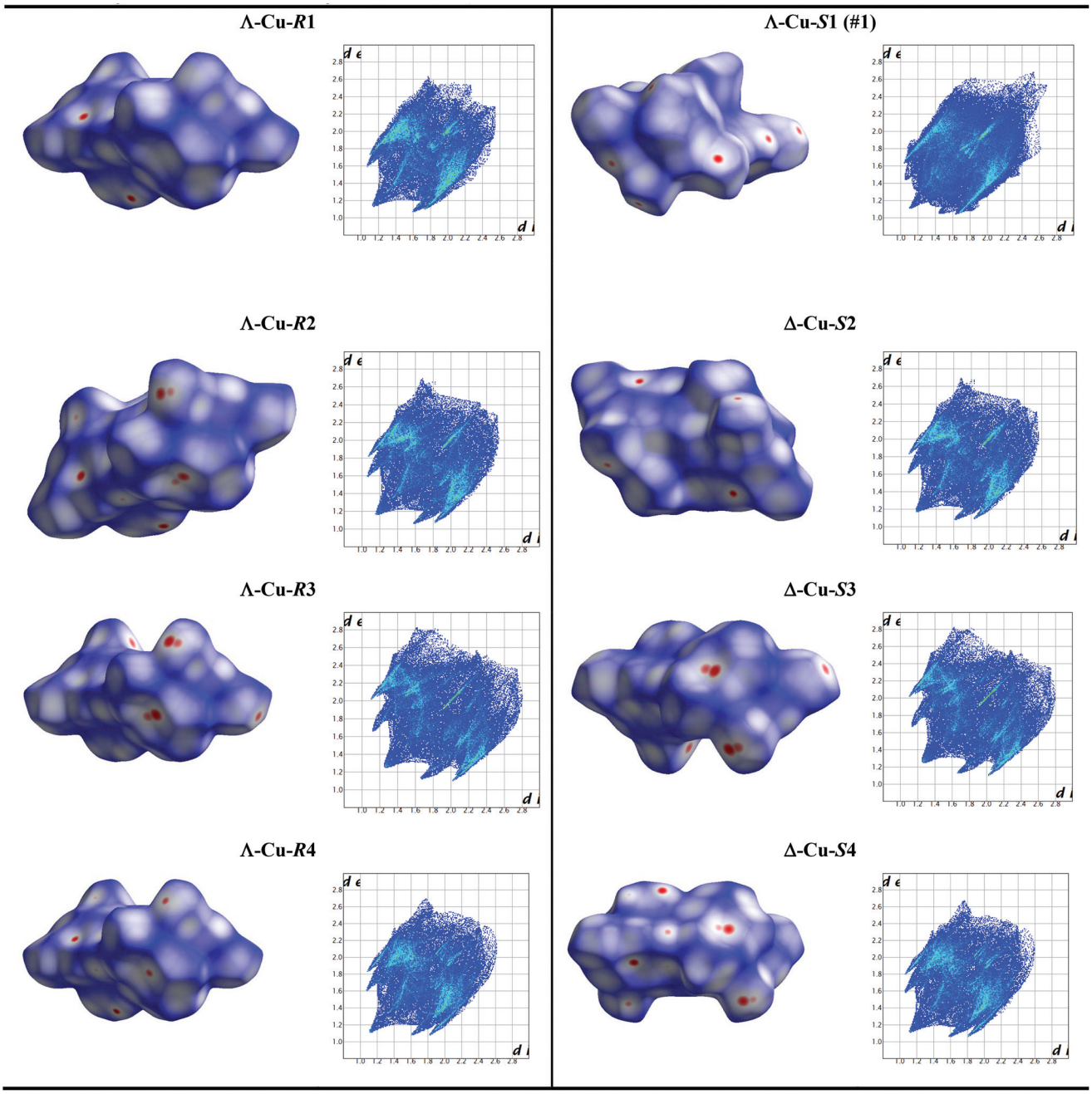

Fig. 4 The graphical illustration of Hirshfeld surfaces with d_{norm} properties and two-dimensional fingerprint plots for the complexes. The strongest intermolecular contacts are shown in red color, while weak contacts as blue color. The d_e (*y*-axis) and d_i (*x*-axis) values are the closest external and internal distances (Å) from given points on the Hirshfeld surfaces contacts.

the series (Table 4), as evidenced by X-ray results (*i.e.*, I···I = 3.3% shorter than vdWr) and by Hirshfeld surface analyses of highest relative contributions to I···I interactions (2.8%) (Fig. 5). The other complexes show relatively weak halogen–halogen interactions with X···X distances higher than those of the sum of van der Waals radii (*i.e.*, X···X = 3.2–10% higher than vdWr) (Table 4).

In the complexes with two different halogen atoms (Λ-Cu-*R*4 and Δ-Cu-*S*4), the hetero–halogen interactions (Br···Cl = 1.4%) are more significant than homo–halogen interactions (Cl···Cl = 0.4%) (Fig. 5). Halogen atoms in the *ortho* position (Br) in two neighbouring molecules (Br···Br) do not show any appropriate interactions between them. It should be noted that the most significant halogen–halogen interactions in all complexes occur between the halogen atoms in the *ortho* positions of a molecule with the halogen atom in the *para* position of neighbour molecule. This observation could be the reason for the absence of intermolecular Br···Br interactions in Λ-Cu-*R*4 and Δ-Cu-*S*4.

Table 4 Geometrical parameters (Å and °) for descriptions of the X···X halogen bonds in the complexes

Definition of geometrical X···X parameters

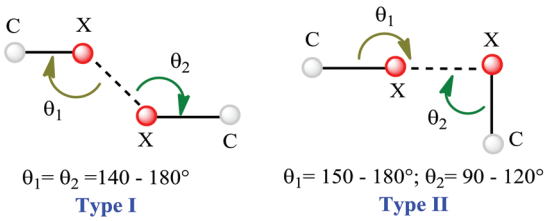

	Λ-Cu-*R*1/Λ-Cu-*S*1[a]	Λ-Cu-*R*2/Δ-Cu-*S*2	Λ-Cu-*R*3/Δ-Cu-*S*3	Λ-Cu-*R*4/Δ-Cu-*S*4
X···X	Cl_1···Cl_2/Cl_3···Cl_4	Br_1···Br_2	I_1···I_2	Br_1···Cl_1
X···X distance (Å)	3.963/3.911	3.819/3.854	3.830/3.829	3.938/3.897
θ_1 (°)	168.19/160.47	166.78/167.37	167.70/167.72	166.44/166.07
θ_2 (°)	110.73/104.95	107.51/108.37	106.45/106.54	108.68/107.43
Deviation from sum of vdW radii (%)	10.0/8.6	3.2/4.1	−3.3/−3.3	9.4/8.2
Type	II	II	II	II

[a] From X-ray structure for Λ-Cu-*S*1 (#1).

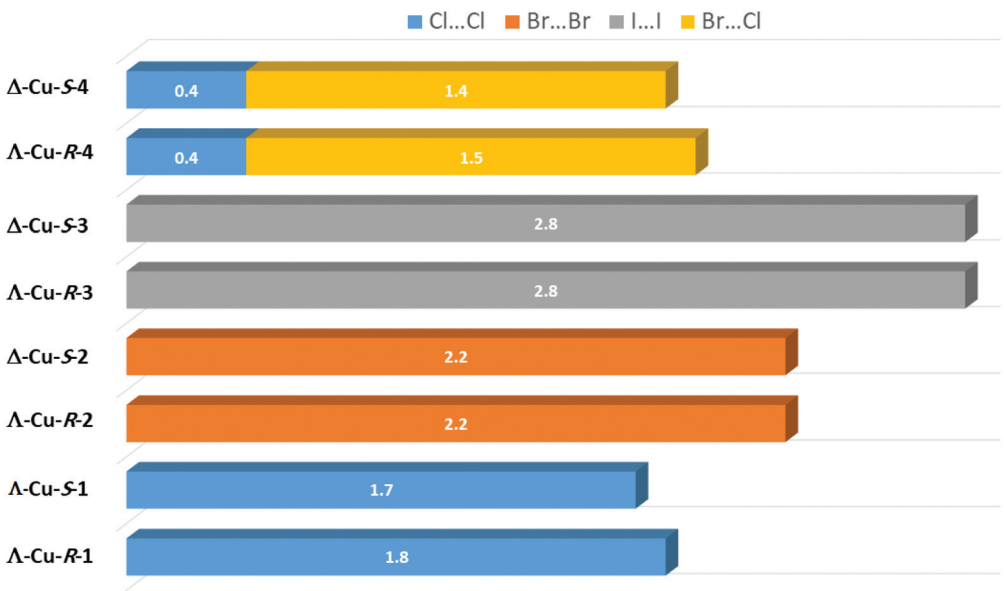

Fig. 5 Relative contributions to the Hirshfeld surfaces area for the halogen–halogen intermolecular interactions (%) in the complexes.

Both Λ-Cu-*R*3 and Δ-Cu-*S*3 crystalize in a C_2 space group and show very similar intermolecular interactions as analysed by the Hirshfeld surfaces (Fig. 4). As shown in Fig. 6a, the halogen atom in the *ortho* position (I1) involves in halogen–halogen interaction with the *para*-halogen of another molecule with a I1···I2 distance of 3.830 Å (Λ-Cu-*R*3) and 3.829 Å (Δ-Cu-*S*3), which is *ca.* 3.3% shorter than the sum of the van der Waals radii of two iodine atoms (4.06 Å) (Table 4). This intermolecular contact is visible as a brilliant red spot on the d_{norm} surface in Fig. 4. Based on the distances (*ca.* 3.830 Å) and angles ($\theta 1/\theta 2$ = *ca.* 167.7/106.5°) in I···I contacts (Table 4), the halogen–halogen interactions can best describe as type II.[27a,b] As shown in Fig. 6a, each molecule (with 4 iodine atoms) can have I···I interactions with four different neighbouring molecules. Similarly, the halogen–halogen interactions are type II in all Λ-Cu-*R*1/Λ-Cu-*S*1, Λ-Cu-*R*2/Δ-Cu-*S*2 and Λ-Cu-*R*4/Δ-Cu-*S*4, respectively.

Apart from halogen···halogen interactions, all complexes except Λ-Cu-*R*1 and Λ-Cu-*S*1 are further linked to each other by the X···π interactions. The geometrical parameters for X···π interactions are listed in Table 5. As shown in Fig. 6b, for example in Λ-Cu-*R*3, the *ortho* iodine atom has an I···π interaction with neighbouring molecules and *vice versa*. According to geometric parameters (Table 5), especially the r_b value which is slightly shorter than the sum of the van der Waals radii of the halogen and carbon atom (*i.e.*, $r_C + r_{Br}$ = 3.55 Å and

 This journal is © The Royal Society of Chemistry 2020

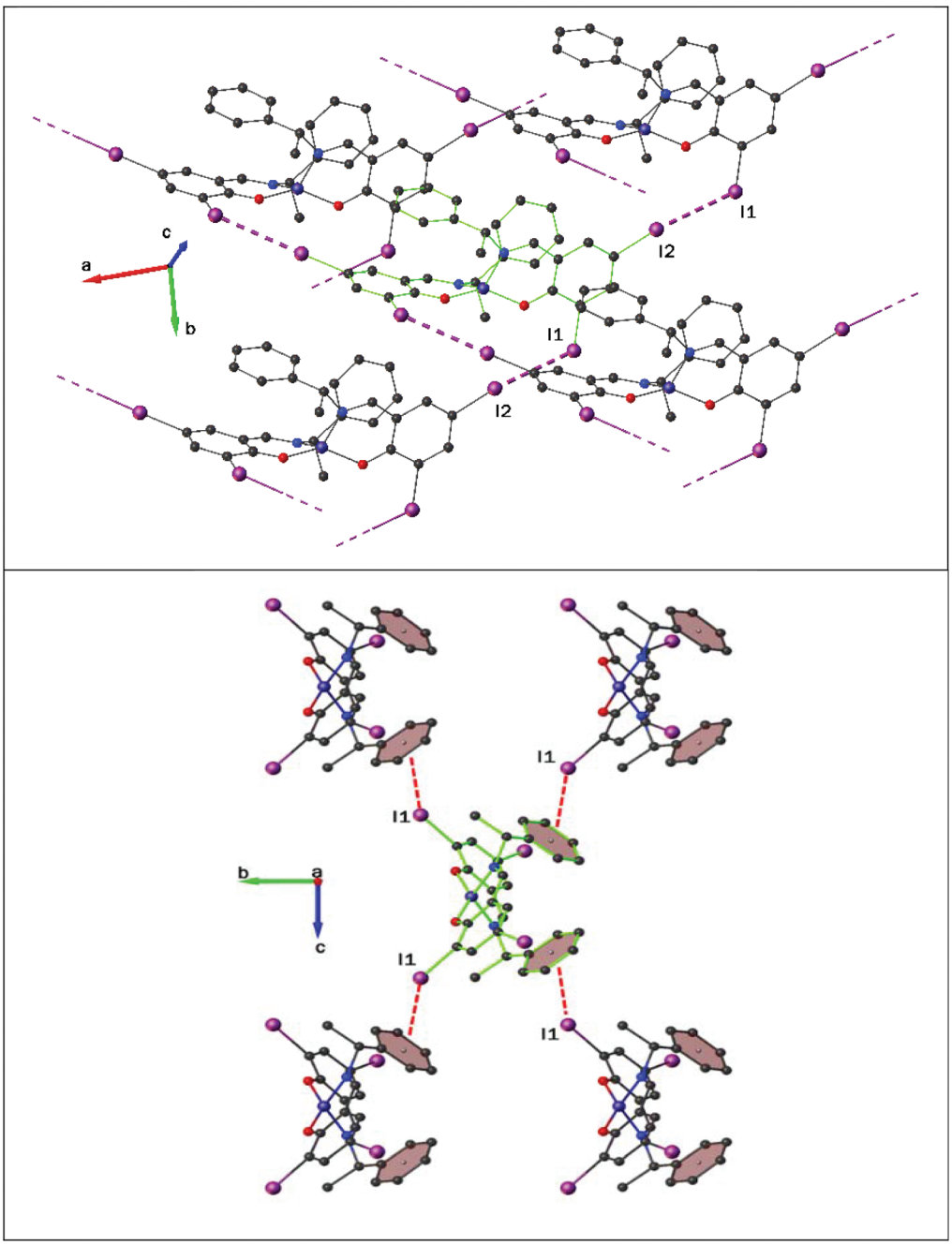

Fig. 6 I···I interactions: a (top) and I···π interactions: b (bottom) in Λ-Cu-*R*3.

$r_C + r_I$ = 3.68 Å), these interactions can be categorized as strong localized (SL) interactions,[27c] evidenced as red spot on the d_{norm} surfaces of all complexes (Fig. 4 and Table 5). In Λ-Cu-*R*4/Δ-Cu-*S*4 with hetero halogen atoms, relatively stronger X···π interaction is seen as a red spot on the d_{norm} surface for Br···π system (Fig. 4 and Table 5).

Experimental electronic spectra (UV-Vis and ECD)

The UV-Vis. spectrum for Cu-*R*2 (Fig. 7) features several strong bands/shoulders below *ca.* 285 nm, assigned to the intra-ligand π → π*/n → π* transitions (LL), and a medium band with absorption maximum at *ca.* 383 nm (λ_{max}), attributed to the metal–ligand (ML) charge transfer transitions. The spectrum further shows a weak broad band in the visible region with λ_{max} at *ca.* 620 nm due to the metal-centred d–d (MM) transitions, a typical band for the copper(II)-core electrons (Fig. 7, inset).[9,11,28a,b,29] The charge neutral complexes are obviously well soluble in non-polar (non-coordinating) to medium polar solvents, and insoluble in highly polar solvents like water. The solution behavior (solvatochromism) of the

Table 5 Geometrical parameters (Å and °) for descriptions of C–X···π interactions in the complexes

Definition of geometrical C–X···π parameters

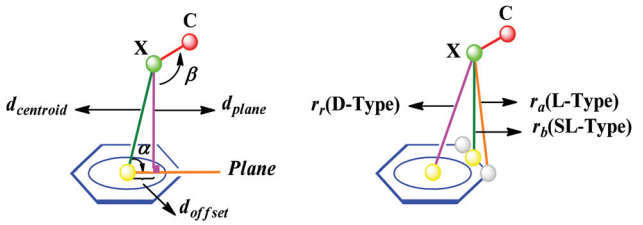

	Λ-Cu-*R*2/Δ-Cu-*S*2	Λ-Cu-*R*3/Δ-Cu-*S*3	Λ-Cu-*R*4/Δ-Cu-*S*4
C–X···π[a]	C–Br_1···π	C–I_1···π	C–Br_1···π
r_r/Å	3.786/3.851	3.829/3.820	3.835/3.764
r_a/Å	3.432/3.498 (C_{11})	3.492/3.492 (C_{11})	3.478/3.410 (C_{11})
r_b/Å	3.39/3.46	3.46/3.46	3.45/3.38
D_{plane}/Å	3.329/3.397	3.413/3.414	3.391/3.325
$d_{centroid}$/Å	3.786/3.851	3.829/3.820	3.835/3.764
d_{offset}/Å	1.803/1.813	1.736/1.712	1.792/1.763
α/°	61.56/61.91	63.04/63.37	62.15/62.07
β/°	147.95/147.62	148.58/148.62	148.12/148.57
Type	SL	SL	SL

[a] π (C_{10}-C_{15}).

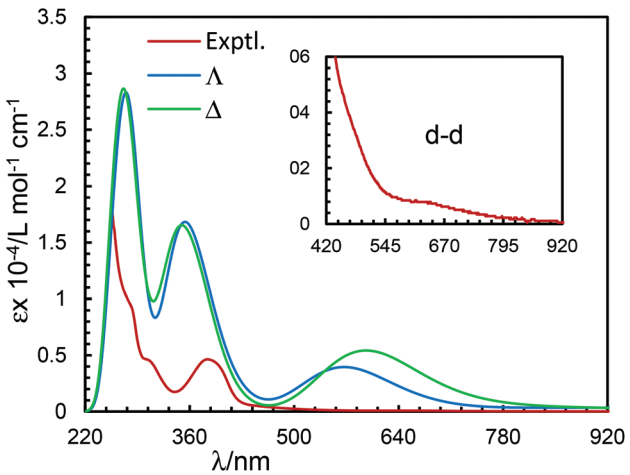

Fig. 7 UV-Vis. spectra for Cu-*R*2 (0.35 mM) in chloroform at 25 °C and simulated spectra for Λ-Cu-*R*2/Δ-Cu-*R*2 at m06/tzvp//b3lyp/6-31G(d) with PCM in chloroform (Gaussian band shape with exponential half-width, σ = 0.33 eV).

complexes was studied by recording absorption spectra in different solvents such as n-hexane, cyclohexane, chloroform, acetone, DMF and DMSO, respectively (Fig. S5a, ESI†). The observed identical spectra, with slightly shifted bands maxima, exclude any coordination of solvent molecules to the metal ion in solution. The results clearly suggest the integrity of the pseudotetrahedral geometry of the copper(II) complexes in solution as at solid-state (discussed above).

Even if we would view the Cu(II) configuration more as square-planar and even if the solid-state to solution helicity inversion with a change of the Λ/Δ configuration at Cu(II) suggests a square-planar transition state, we note that Cu(II) with its d^9 electron configuration is subject to Jahn–Teller distortion. The Jahn–Teller effect at a square-planar Cu(II) complex leads to only very weak binding of axial ligands with elongated Cu···ligand distances. Indeed, solution studies reveal a negative solvatochromic behavior with shifting the MLCT bands maxima (λ/max) to the higher energies (blue shift by *ca.* 6 nm) in the solvent of increasing polarity or dipole moment[28d] (Fig. S5b, ESI†), indicating that the MLCT bands are charge transfer in nature.[5c–e,28a–c,29]

The electronic circular dichroism (ECD) spectra for the enantiomeric pairs Cu-*S*2/Cu-*R*2 and Cu-*S*4/Cu-*R*4 were measured in chloroform at 25 °C (Fig. 8), exhibit consistent similarities along the series. The ECD spectra feature several bands with opposite Cotton effect, associated to the MM, ML and LL electronic transitions, respectively. Indeed, the observed mirror-image relationships of these bands, along the measured spectral range, indicate enantiomeric excess of the *S* or *R*-ligated complexes in solution. The spectra for *S*-/*R*-ligated

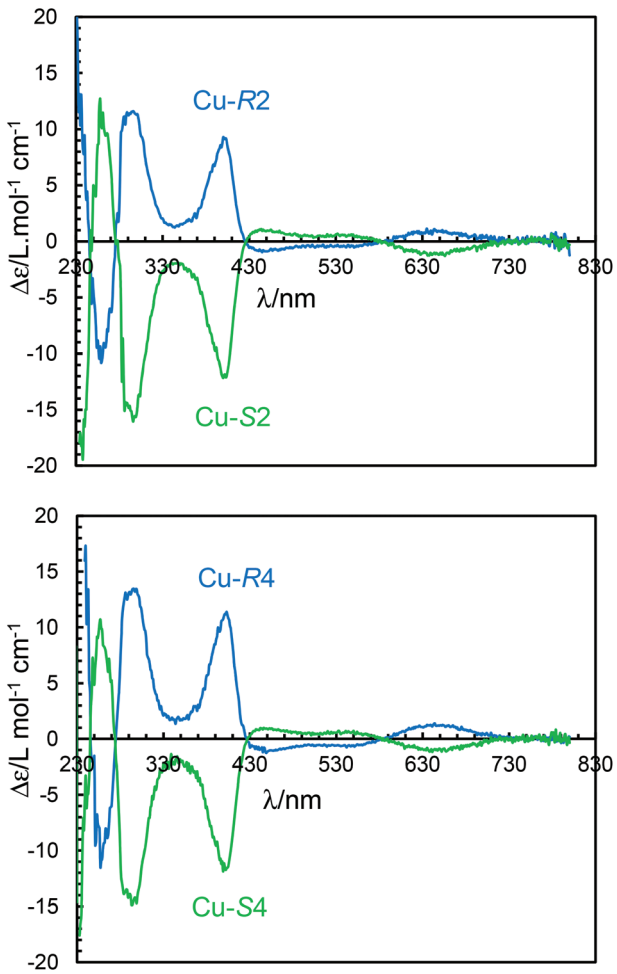

Fig. 8 Electronic circular dichroism (ECD) spectra for the enantiomeric pairs Cu-*R*2/Cu-*S*2 (1.95/2.05 mM) and Cu-*R*4/Cu-*S*4 (3.24/2.10 mM) in chloroform at 25 °C (cell path-length: 1.0 mm).

 This journal is © The Royal Society of Chemistry 2020

complexes are characterized by the following series of bands (sign and strength) at *ca.* 650 nm (−/+, weak), 540 nm (+/−, weak), 450 nm (+/−, weak), 400 nm (−/+, strong), *ca.* 300 nm (−/+, strong) and 260 nm (+/−, strong), respectively. Similar results of ECD spectral patterns were reported for the analogous M(II)-*chiral*-salicylaldimine/-oxo-naphthaldimine complexes (M = Fe, Co, Ni, Cu, Zn).[8–11]

Optimized structures and excited state properties

The gas phase DFT optimized structures (Fig. S6, ESI†) for the diastereomeric pairs Λ-Cu-*R*1/Δ-Cu-*R*1, Λ-Cu-*S*1/Δ-Cu-*S*1, Λ-Cu-*R*2/Δ-Cu-*R*2, Λ-Cu-*S*2/Δ-Cu-*S*2, Λ-Cu-*R*4/Δ-Cu-*R*4 and Λ-Cu-*S*4/Δ-Cu-*S*4 at b3lyp/6-31g(d) show that the Δ-Cu-*R* diastereomer is slightly more stable than Λ-Cu-*R* by 1–3 kcal mol^{-1} and Λ-Cu-*S* is slightly more stable than Δ-Cu-*S* by 1–5 kcal mol^{-1}. The excited state properties by TDDFT were calculated at m06/tzvp//b3lyp/6-31G(d) with PCM in chloroform as solvent for diastereomeric pairs Λ-Cu-*R*2/Δ-Cu-*R*2 and Λ-Cu-*S*2/Δ-Cu-*S*2, respectively. The simulated UV-Vis. and ECD spectra (Fig. 9 and S7†) are comparable to the experimental spectra with slightly shifted bands maxima (Fig. 7 and 9). The differences in band maxima and sign of Δε between the experimental and simulated spectra reflect certain drawbacks of the TDDFT protocol such as overestimation of excitation energies, presence of low energy states with low oscillator strengths, improper descriptions and/or long distances of charge-transfer processes, *etc.*[30] In addition, proper choices of the functionals and basis sets, DFT optimizations in the gas (instead of the solution) phase and limitations of experimental works (*e.g.*, solute and solvent interactions, and dissociation-equilibria for the labile tetrahedral/square-planar complexes in solution) enhance these differences.[8,9,13,18]

The simulated ECD spectra reveal the expected mirror-image relationships with opposite Cotton effect for each diastereomeric pair (Fig. 9), alike the experimental spectra for the enantiomeric excess pairs Cu-*R*2/Cu-*S*2 and Cu-*R*4/Cu-*S*4 (Fig. 8). The overall nature of *chirality* of metal-complexes is reflected on their ECD spectra, which in particular determines the absolute configuration of the metal centre by d–d transitions bands in the visible region.[3b,8–11] Indeed, combined analyses of experimental and simulated ECD spectra have successfully been used to predict the absolute configuration of the metal centre (Λ *vs.* Δ) resulting from diastereoselection and induced chirality by the *S*- or *R*-ligands.[8–12] Thus, comparisons of experimental and simulated spectra for Λ-Cu-*R*2/Δ-Cu-*R*2 or Λ-Cu-*S*2/Δ-Cu-*S*2 reveal that the spectra for Cu-*R*2 or Cu-*S*2 are comparable to Δ-Cu-*R*2 or Λ-Cu-*S*2 with slightly shifted bands maxima (Fig. 9). These results, however, suggest that the complex Cu-*R*2 or Cu-*S*2 corresponds well to the diastereomeric excess for Δ-Cu-*R*2 or Λ-Cu-*S*2 in solution. A dynamic equlibrium with diastereomeric excess for Δ-M-*R* or Λ-M-*S* and *vice versa* (*i.e.*, Λ-M-*R* or Δ-M-*S*) prevails in solution, as evinced by variable time and/or temperature dependent ^{1}H NMR and ECD/VCD analyses.[8–12] The ECD results (experimental and simulated) thus corroborate that the diastereoselection and induced chirality at-metal lead to preferred formation of Δ-Cu-*R* or Λ-Cu-*S* (*i.e.*, diastereomeric excess) in solution. These results are in good accord with the slightly more stable optimized (gas phase) structures for Δ-Cu-*R* or Λ-Cu-*S* diastereomers (Fig. S6, ESI†). On the contrary, solid state X-ray structures show preferred formation of Λ-Cu-*R* or Δ-Cu-*S* (as major diastereomer) for *R* or S-ligated complexes, as discussed above. Thus, solid-state *versus* solution studies suggest helicity inversion from Λ-Cu-*R* or Δ-Cu-*S* (at solid-state) to Δ-Cu-*R* or Λ-Cu-*S* (in solution), as evidenced in the analogous bis[(*R*)-*N*-1-(*p*-X-Ar)ethyl-(salicylaldiminato-κ^{2}N,O]-Δ/Λ-Cu(II) with X = OCH_3.[11]

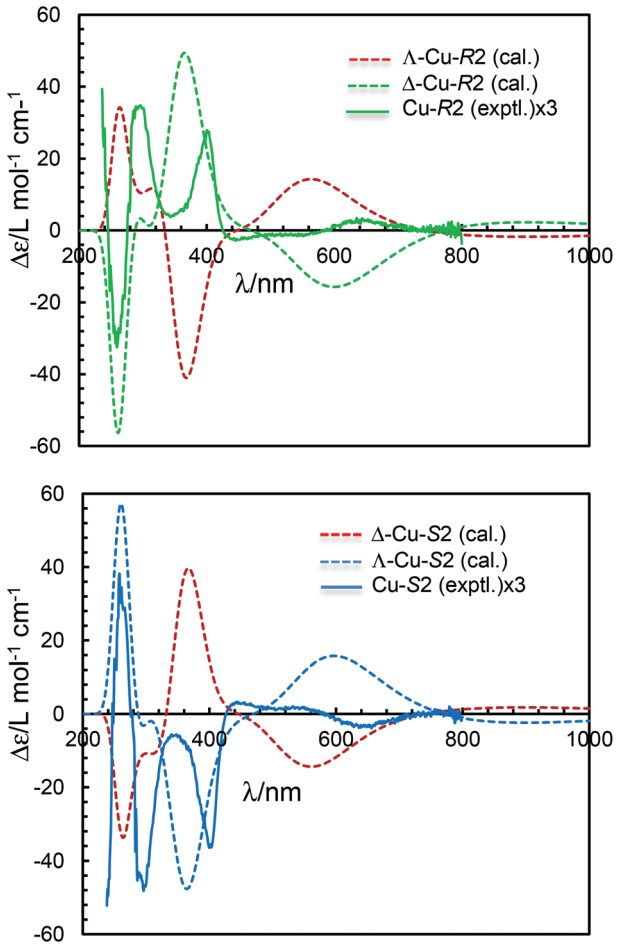

Fig. 9 Comparisons of experimental and simulated ECD spectra: (a) experimental spectra (solid line) for Cu-*R*2 (1.95 mM) and Cu-*S*2 (2.05 mM) in chloroform at 25 °C ($\Delta\varepsilon_{exptl.}$ values are increased by 3 times) and (b) simulated spectra (dashed line) for diastereomeric pairs Λ-Cu-*R*2/Δ-Cu-*R*2 and Λ-Cu-*S*2/Δ-Cu-*S*2 at m06/tzvp//b3lyp/6-31G(d) with PCM in chloroform, respectively (Gaussian band shape with exponential half-width σ = 0.33 eV).

It was also attempted to assign the electronic spectra based on orbitals and populations analyses of excited state properties for Δ-Cu-*R*2. Some selected and simplified assignments on simulated spectra are listed in Table 6, which are comparable to the experimental data in solution. A combined band comprising of MM, ML and LL transitions is found at 596 nm

Table 6 Some selected and simplified assignments on electronic spectra for Δ-Cu-R2, calculated at m06/tzvp//b3lyp/631g(d) with PCM in chloroform[a]

λ/nm[b]	Oscill. strength. (f)	Transitions[c]	Assignments[d]
596 (620)	0.1101	H-8 → L, H → L	MM, ML, LL
371 (383)	0.1073	H-1 → L+1, H → L+2	MM, ML
339 (310)	0.2108	H-8 → L, H → L+2	ML, ML, LL
279 (285)	0.1034	H-5 → L+2, H-3 → L	ML, LL
255	0.1016	H-21 → L, H-18 → L	ML, LL

[a] Assigned for β-spin MOs considerations. [b] Experimental data for Cu-*R*2 in chloroform are in parentheses. [c] H/L = HOMO/LUMO. [d] MM = d–d, ML = metal–ligand and LL = intra-ligand transitions, respectively.

(λ_{max}), very close to experimental band at *ca.* 620 nm, with significant amount of oscillator strength (f = 0.1101) for HOMO to LUMO transitions (Fig. 10).

Thermal behavior

Thermally induced phase transformation from crystalline (at low temperature) to isotropic liquid phase (at high temperature) is well documented in transition metal-Schiff base complexes, which can be analyzed by differential scanning calorimetry (DSC).[5b–d,8–10] The thermal behavior (DSC curves) for each enantiomeric pair are essentially identical and show exothermic peaks at 145–219 °C with significant amount of heat of transformation (ΔH = 37.19–52.23 kJ mol^{-1}) (Fig. 11 and Table 7). The transformation temperature increases with increasing molecular weight of the complexes with the substituents groups following the sequence of Cl < ClBr < Br < I. On the other hand, the cooling curves show no corresponding peaks on the reverse direction. Thus, thermal analyses suggest an irreversible phase transformation from crystalline to isotropic liquid phase.

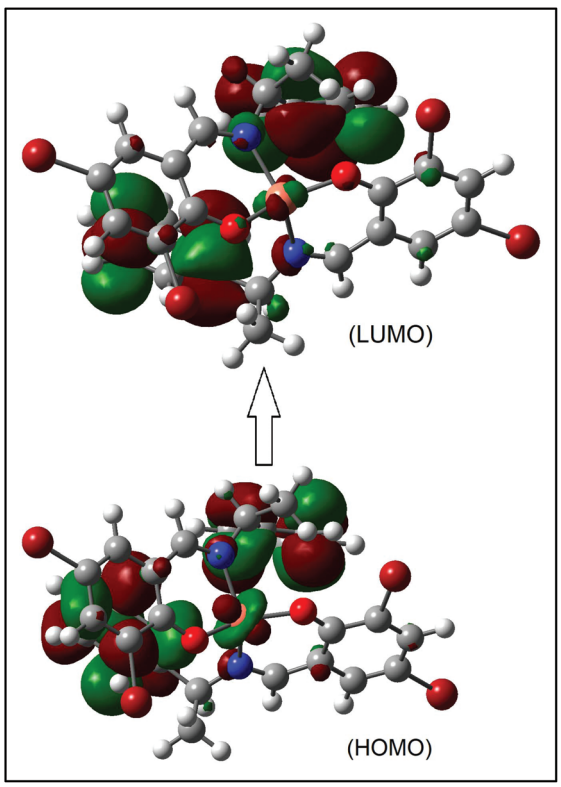

Fig. 10 HOMO and LUMO for Δ-Cu-*R*2, calculated at m06/tzvp//b3lyp/631g(d) with PCM in chloroform for β-spin considerations.

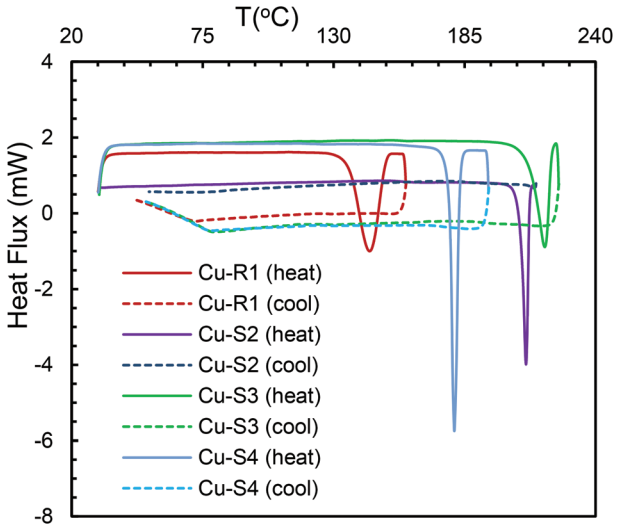

Fig. 11 Differential scanning calorimetry (DSC) curves for the complexes.

EPR spectra

The X-band EPR spectra for paramagnetic copper(II)-Schiff bases complexes were measured in CH_2Cl_2 at *ca.* 100 K (Fig. 12). The spin Hamiltonian parameters, obtained by simulation,[31a] are listed in Table 8 and spectra are included in Fig. S9, ESI.† All spectra show axial symmetry with $g_z > g_{x,y} > 2.0$. The values obtained for the ratio $g_z/A_z \geq 135$ cm suggest pseudotetrahedral geometry for the investigated complexes.[31] Both the d_{z^2} and $d_{x^2-y^2}$ orbitals are filled at ground-state, as shown in Fig. 10, which are in agreement with the EPR parameters and suggest tetrahedral distortions.

Table 7 Differential scanning calorimetry (DSC) data for the complexes[a]

Complexes	Heating curve peak temp. (°C)/ΔH[b]	Cooling curve
Cu-*R*1	145.11/−37.19	No peak
Cu-*S*2	210.79/−52.23	No peak
Cu-*S*3	218.66/−41.43	No peak
Cu-*S*4	180.67/−38.82	No peak

[a] DSC was run just before the decomposition temperature of the complexes. [b] ΔH = heat of transformation in kJ mol^{-1}.

This journal is © The Royal Society of Chemistry 2020

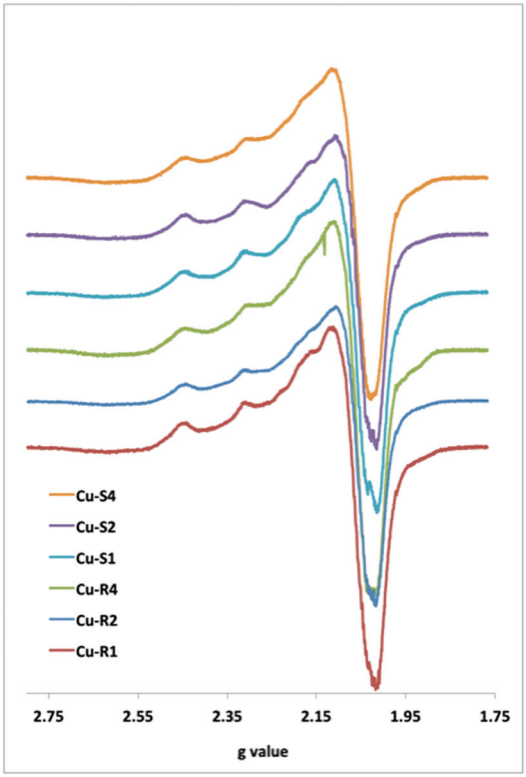

Fig. 12 X-band EPR spectra of the copper(II)-complexes in CH_2Cl_2 (*ca.* 3.0 mM) at *ca.* 100 K.

Table 8 Spin Hamiltonian parameters obtained by simulation of the experimental spectra for the copper(II)-complexes in CH_2Cl_2 (*ca.* 3.0 mM)

Complexes	$g_{x,y}$	g_z	$A_{x,y} \times 10^4$ cm^{-1}	$A_z \times 10^4$ cm^{-1}	g_z/A_z cm
Cu-*R*1	2.064	2.250	24.4	166.0	136
Cu-*R*2	2.064	2.249	20.6	165.9	136
Cu-*R*4	2.066	2.248	18.5	166.9	135
Cu-*S*1	2.063	2.246	23.6	166.7	135
Cu-*S*2	2.064	2.249	20.9	166.9	135
Cu-*S*4	2.068	2.247	18.4	166.8	135

Conclusions

An induced Δ or Λ-chirality at-metal has been established along the C_2-axis of pseudotetrahedral bis[(*S* or *R*)-*N*-1-(phenyl)ethyl-(2,4-X^1,X^2-salicylaldiminato-κ^{2}N,O]-Δ/Λ-Cu(II). Steric constraints by halogen substituents on the coordinating salicylal-ring provide diastereoselectively Λ-Cu-*R* or Δ-Cu-*S* as major diastereomer and Δ-Cu-*R* or Λ-Cu-*S* as minor diastereomer at solid-state. The results suggest inversion of induced chirality at-metal in contrast to those reported in the analogous complexes without halogen substituents. The observed mirror-image relationships of ECD spectra indicate enantiomeric excess of *R* or *S*-ligated complexes in solution. Comparisons of experimental and simulated ECD spectra suggest Cu-*R* or Cu-*S* correspond to diastereomeric excess of Δ-Cu-*R* or Λ-Cu-*S* in solution. Optimized structures at gas phase also reveal Δ-Cu-*R* or Λ-Cu-*S* slightly more stable. The solid-state *versus* solution (or gas phase) studies indicate an interconversion of induced chirality (helicity inversion) at-metal from Λ-Cu-*R* or Δ-Cu-*S* to Δ-Cu-*R* or Λ-Cu-*S* diastereomers. EPR spectra along with simulation show an axial symmetry and spin Hamiltonian parameters supporting pseudotetrahedral geometry for the complexes. The present results demonstrate that the steric constraints by halogen substituents on the salicylal rings and the solid-state *versus* solution (or gas-phase) studies efficiently control the stereochemical induction at-metal and lead to helicity inversion in *chiral* copper(II)-2,4-dihalo-salicylaldiminate with pseudotetrahedral geometry. These results are of particular interest to synthesize *chiral*-at-metal complexes and to use them as potential *chiral*-catalysts in a stereoselective way.

Experimental

Copper(II) chloride, 3,5-dibromosalicylaldehyde, 3,5-diiodosalicylaldehyde, 3,5-dichlorosalicylaldehyde, 3-bromo-5-chlorosalicylaldehyde, (*R*)-(+)-α-methylbenzylamine and (*S*)-(−)-α-methylbenzylamine were purchased from Sigma-Aldrich and used without further purification. Commercial solvents were distilled and used for preparation of ligands and complexes. FT-IR spectra were recorded on a JASCO, FT/IR-6300 spectrometer (4000–400 cm^{-1}) in KBr pellets. ^{1}H and ^{13}C NMR spectra were recorded on a Bruker Avance III 400 spectrometer. The elemental analysis was performed on Leco, CHNS-932 and PerkinElmer 7300 DV elemental analyzers. UV-Visible spectra were recorded with a Shimadzu UV 1800 spectrophotometer in chloroform at 25 °C. Differential Scanning Calorimetery (DSC) were run on a Shimadzu DSC-60 in the range 30–230 °C (just up to decomposition temperature) with a rate of 10 K min^{-1} under nitrogen atmosphere. The molar conductance was measured using Mettler Toledo Fivego (Model F3) conductivity meter in dimethyl formamide (DMF) at 25 °C. ECD spectra were obtained with JASCO Spectropolarimeter (J 810) in choloroform at *ca.* 25 °C. The X-band EPR spectra of frozen solutions (frozen in liquid nitrogen, *ca.* 100 K) of the complexes were recorded on a Bruker ESP 300E spectrometer. The spectrometer was operated at 9.51 GHz with a frequency modulation of 100 kHz.

General procedure for ligand synthesis

All chiral Schiff-base ligands were synthesized using identical reaction conditions *via* condensation of the enantiopure amine, (*R*)-(+)-α-methylbenzylamine or (*S*)-(−)-α-methylbenzylamine with the appropriately di-substituted halogen-salicylaldehyde in aqueous solution.[19] Although these ligands could be synthesized in various solvents such as ethanol, methanol and chloroform, the highest and purest yield was achieved in water. Here only the synthesis of *R*-H1 is described in detail. To a solution of 3,5-dichlorosalicylaldehyde

(1 mmol) in distilled water (10 mL) was added (*R*)-(+)-α-methylbenzylamine (1.2 mmol). A yellow precipitate resulted, and this solution mixture was stirred for *ca.* 6 h at room temperature. The product was filtered off, washed with 100 ml distilled water and dried at room temperature to afford a yellow precipitate in high yield (<90%, based on aldehydes). Both the *R*- and *S*-enantiomers show identical IR and ^{1}H NMR spectra.

***R*-H1 and *S*-H1.** Yield 91 and 93%, respectively. Anal. calcd for $C_{15}H_{13}Cl_2NO$: C, 61.24; H, 4.45; N, 4.76. Found for *R*-H1: C, 61.21; H, 4.43; N, 4.77%.; Found for *S*-H1: C, 61.20; H, 4.45; N, 4.79%. ^{1}H-NMR [400 MHz, $CDCl_3$] δ (ppm): 14.73 [s, 1H, O*H*], 8.30 [s, 1H, C*H*N], 7.42–7.15 [m, 7H, Ar-*H*], 4.66 [q, 1H, C*H*] and 1.68 [d, 3H, CH_3]. ^{13}C-NMR [100 MHz, $CDCl_3$] δ (ppm): 161.2 (*C*HN), 156.3, 142.3, 131.7, 128.6, 127.2, 125.9, 122.4, 121.9, 118.8 (Ar-*C*), 67.1 (*C*H) and 24.1 (CH_3). IR (KBr, cm^{-1}): 3434 m (br, νO–H), 3064, 2980w (νC–H) and 1629vs (νC=N).

***R*-H2 and *S*-H2.** Yield 94 and 95%, respectively. Anal. calcd for $C_{15}H_{13}Br_2NO$: C, 47.03; H, 3.42; N, 3.66. Found for *R*-H2: C, 46.98; H, 3.44; N, 3.62%.; Found for *S*-H2: C, 47.01; H, 3.43; N, 3.63%; ^{1}H-NMR [400 MHz, $CDCl_3$] δ (ppm): 14.89 [s, 1H, O*H*], 8.27 [s, 1H, C*H*N], 7.71–7.28 [m, 7H, Ar-*H*], 4.65 [q, 1H, C*H*] and 1.67 [d, 3H, CH_3]. ^{13}C-NMR [100 MHz, $CDCl_3$] δ (ppm): 161.7 (*C*HN), 158.6, 142.5, 138.0, 132.9, 119.9, 112.6, 109.2 (Ar-*C*), 67.4 (*C*H) and 24.5 (CH_3). IR (KBr, cm^{-1}): 3434 m (br, νO–H), 3058, 2977w, (νV–H) and 1627vs (νC=N).

***R*-H3 and *S*-H3.** Yield 89 and 92%, respectively. Anal. calcd for $C_{15}H_{13}I_2NO$: C, 37.76; H, 2.75; N, 2.94. Found for *R*-H3: C, 37.80; H, 2.77; N, 2.97%.; Found for *R*-H3: C, 37.79; H, 2.78; N, 2.93%. ^{1}H-NMR [400 MHz, $CDCl_3$] δ (ppm): 15.01 [s, 1H, O*H*], 8.15 [s, 1H, C*H*N], 8.08–7.28 [m, 7H, Ar-*H*], 4.67 [q, 1H, C*H*] and 1.68 [d, 3H, CH_3]. ^{13}C-NMR [100 MHz, $CDCl_3$] δ (ppm): 161.0 (*C*HN), 148.2, 141.7, 139.4, 128.4, 127.3, 126.0, 119.0 (Ar-*C*), 66.4 (*C*H) and 23.8 (CH_3). IR (KBr, cm^{-1}): 3432 m (br, νO–H), 2922w (νC–H) and 1625vs (νC=N).

***R*-H4 and *S*-H4.** Yield 92% for both ligands. Anal. calcd for $C_{15}H_{13}BrClNO$: C, 53.20; H, 3.87; N, 4.14. Found for *R*-H4: C, 53.14; H, 3.83; N, 4.09%.; Found for *S*-H4: C, 53.17; H, 3.83; N, 4.12%. ^{1}H-NMR [400 MHz, $CDCl_3$] δ (ppm): 14.84 [s, 1H, O*H*], 8.28 [s, 1H, C*H*N], 7.59–7.20 [m, 7H, Ar-*H*], 4.65 [q, 1H, C*H*] and 1.68 [d, 3H, CH_3]. ^{13}C-NMR [100 MHz, $CDCl_3$] δ (ppm): 161.7 (*C*HN), 158.0, 142.5, 135.1, 129.8, 128.2, 127.7, 126.4, 122.8, 119.1, 112.2 (Ar-*C*), 67.5 (*C*H) and 24.6 (CH_3). IR (KBr, cm^{-1}): 3433 m (br, νO–H), 3062, 2924w (νC–H) and 1628vs (νC=N).

General procedure for complex synthesis

A general synthetic route was used for all complexes in which $CuCl_2$ (1 mmol) was dissolved in 2 mL of MeOH and then added to a methanolic solution (30 mL) containing the appropriate Schiff base ligands (2 mmol).

Cu-*R*1 and Cu-*S*1. After addition of $CuCl_2$ to a solution of the ligands, the color of the solution changed from yellow to brown without any precipitation and was refluxed for *ca.* 4 h. The solution was then allowed to stand at room temperature affording dark brown crystals by slow evaporation of the solvent. Yield 75 and 81% for Cu-*R*1 and Cu-*S*1, respectively. Anal. Calc. For $C_{30}H_{24}Cl_4CuN_2O_2$: C, 55.45; H, 3.72; N, 4.31%. Found for Cu-*R*1: C, 55.40; H, 3.71; N, 4.32%. Found for Cu-*S*1: C, 55.43; H, 3.70; N, 4.34%. IR data (KBr, cm^{-1}): 3436 m (br, νH_2O), 3032, 2974 m (νC–H) and 1608vs (νC=N). Λ_m (DMF) = 0.65 S cm^2 mol^{-1} (0.42 mM) for Cu-*R*1.

Cu-*R*2 and Cu-*S*2. After addition of $CuCl_2$ to a solution of the Schiff bases, a brown precipitate was formed quickly. It was collected by filtration, washed with cold methanol and dried in air. Dark brown single crystals were obtained on slow evaporation of the solvent from a solution of the sample in chloroform and methanol (70 : 30, v/v). Yield 83 and 80% Cu-*R*2 and Cu-*S*2, respctively. Anal. Calc. For $C_{30}H_{24}Br_4CuN_2O_2$: C, 43.53; H, 2.92; N, 3.38%. Found for Cu-*R*2: C, 43.56; H, 2.94; N, 3.41%. Found for Cu-*S*2: C, 43.54; H, 2.91; N, 3.39%. IR data (KBr, cm^{-1}): 3434 m (br, νH_2O), 3035, 2972 m (νC–H) and 1604vs (νC=N). Λ_m (DMF) = 0.55 S cm^2 mol^{-1} (0.48 mM) for Cu-*S*2.

Cu-*R*3 and Cu-*S*3. After addition of $CuCl_2$ to a solution of the Schiff bases, a brown precipitate was formed. It was filtered, washed with cold methanol and dried in air. Dark brown single crystals were obtained on slow evaporation of the solvent from a solution of the sample in chloroform and methanol (50 : 50, v/v). Yield 80 and 77% for Cu-*R*3 and Cu-*S*3, respectively. Anal. Calc. For $C_{30}H_{24}I_4CuN_2O_2$: C, 35.48; H, 2.38; N, 2.76%. Found for Cu-*R*3: C, 35.50; H, 2.37; N, 2.76%. Found for Cu-*S*3: C, 35.49; H, 2.36; N, 2.77%. IR data (KBr, cm^{-1}): 2963w (νC–H) and 1600vs (νC=N). Λ_m (DMF) = 1.46 S cm^2 mol^{-1} (*ca.* 0.39 mM) for Cu-*R*3.

Cu-*R*4 and Cu-*S*4. After addition of $CuCl_2$ to a solution of the Schiff bases, the color changed from yellow to brown without any precipitation and therefore, the solution was refluxed for *ca.* 4 h. It was then allowed to stand at room temperature affording dark brown crystals by slow evaporation of the solvent. Yield: 79 and 88% for Cu-*R*4 and Cu-*S*4, respectively. Anal. Calc. For $C_{30}H_{24}Br_2Cl_2CuN_2O_2$: C, 48.77; H, 3.28; N, 3.79%. Found for Cu-*R*4: C, 48.75; H, 3.28; N, 3.81%. Found for Cu-*S*4: C, 48.76; H, 3.28; N, 3.80%. IR data (KBr, cm^{-1}): 3432 m (br, νH_2O), 3045, 2974 m (νC–H) and 1606vs (νC=N). Λ_m (DMF) = 1.80 S cm^2 mol^{-1} (*ca.* 0.54 mM) for Cu-*R*4.

X-ray crystallography

X-ray data for Λ-Cu-*S*1 (#1) and Δ-Cu-*S*4 were collected on a Rigaku SuperNova dual system in combination with Atlas type CCD detector using the CuK_α radiation (1.54184 Å) at *ca.* 140 K. The data reduction was carried out by *CrysAlis*^{Pro}.[32] The dataset was reduced by EvalCCD[33] and then corrected for absorption.[34] X-ray data for Λ-Cu-*S*1 (#2), Λ-Cu-*R*1, Λ-Cu-*R*3, Λ-Cu-*R*4, Δ-Cu-*S*2 and Δ-Cu-*S*3 were collected with a Bruker APEX II CCD area detector diffractometer using the MoK_α radiation (λ = 0.71073 Å) at *ca.* 298 K or 273 K. Data collections, cell refinements, data reductions and absorption corrections were performed using multiscan methods with Bruker software.[35] The solutions and refinements were performed by *SHELXT*[36] and *SHELXL*,[37] respectively. The crystal structures were refined using full-matrix least-squares based on F^2 with all non-hydrogen atoms anisotropically defined. Hydrogen

 This journal is © The Royal Society of Chemistry 2020

atoms were placed in calculated positions by means of the "riding" model. The data for Λ-Cu-*R*2 was collected on a Bruker D8 QUEST ECO diffractometer using the MoK_α radiation (λ = 0.71073 Å) at *ca.* 150 K. All diffractometer manipulations were carried out using Bruker APEX3 software.[38] Structure solution and refinement was carried out using XS, XT and XL software, embedded within the Bruker SHELXTL suite.[39] For each structure, the absence of additional symmetry was confirmed using ADDSYM incorporated in the PLATON program. While essentially diastereomerically pure compounds were obtained based on the crystallography, in certain cases (CCDC numbers 1943411–1943414 and 1943419†) the determined Flack parameters were found to be greater than zero within error. Hence, the data was treated as a two-component inversion twin in order to deal with the level B alert that otherwise would be raised in the CHECKCIF protocol. It should be noted that the fractional contribution of the inverted component (as indicated by the BASF value which then is equal to the Flack parameter) is in all cases very small (Tables 9 and 10) and does not, in our opinion, impact the conclusions drawn from the solution state studies. For example, when the data set for Λ-Cu-*R*2 (R-Br2 + Cu) was re-refined without TWIN/BASF instruction, the Flack parameter was 0.032(5), thereby generating a level B alert. With the TWIN/BASF instruction the Flack parameter became 0.025(8) (Table 9) without level B alert in the CHECKCIF. More details concerning the crystal structures and their refinements can be found in Tables 9 and 10 or in the corresponding CIF files (ESI†).

Computational methods

To rationalize experimental results and gain detailed insights into diastereoselection and induced chirality at-metal centre (Λ *vs.* Δ), the optimized structures and excited state properties were performed using the Gaussian 09.[40] The initial gas phase equlibrium geometries for the enantiomeric pairs Λ-Cu-*R*1/Λ-Cu-*S*1, Λ-Cu-*R*2/Δ-Cu-*S*2 and Λ-Cu-*R*4/Δ-Cu-*S*4 were generated from the corresponding X-ray structures. The geometries for opposite configured structures (*i.e.*, for Δ-Cu-*R*1/Δ-Cu-*S*1, Δ-Cu-*R*2/Λ-Cu-*S*2 and Δ-Cu-*R*4/Λ-Cu-*S*4) were designed by mirror inversion of the complexes following manual inversion of each carbon chiral center.[8–10] The geometry around the metal atom was taken fixed by constraining Cu–O/Cu–N bond lengths and O–Cu–O/N–Cu–N angles at their respective values from the X-ray structures.[10] All remaining rotatable bonds/angles were included in geometry optimization process. Finally, the structures for diastereomeric pairs Λ-Cu-*S*1/Δ-Cu-*S*1, Λ-Cu-*R*1/Δ-Cu-*R*1, Λ-Cu-*R*2/Δ-Cu-*R*2, Λ-Cu-*S*2/Δ-Cu-*S*2, Λ-Cu-*R*4/Δ-Cu-*R*4 and Λ-Cu-*S*4/Δ-Cu-*S*4 were optimized by DFT at b3lyp/6-31g(d), respectively (see structures in Fig. S6, ESI†). Further, geometry optimization was performed allowing all bonds/angles freely rotatable around the metal ion as well as in the whole structure. The results show similar trend of free energy change for each diastereomeric pair in both optimization methods.

The excited state properties by TDDFT were determined with different combinations of the functionals (b3lyp, cam-

Table 9 Crystal data and structures refinement details

	Λ-Cu-*R*1	Λ-Cu-*R*2	Λ-Cu-*R*3	Λ-Cu-*R*4
Data set	*R*-Cl2 + Cu	*R*-Br2 + Cu	*R*-I2 + Cu	*R*-ClBr + Cu
Empirical formula	$C_{30}H_{24}Cl_4CuN_2O_2$	$C_{30}H_{24}Br_4CuN_2O_2$	$C_{30}H_{24}I_4CuN_2O_2$	$C_{30}H_{24}Br_2Cl_2CuN_2O_2$
M (g mol^{-1})	649.85	827.69	1015.65	738.77
Temperature (K)	298(2)	150(2)	273(2)	298(2)
Wavelength (Å)	0.71073	0.71073	0.71073	0.71073
Crystal system	Monoclinic	Monoclinic	Monoclinic	Monoclinic
Space group	*C*2	*C*2	*C*2	*C*2
a (Å)	13.976(3)	14.1169(5)	14.5586(3)	14.040(3)
b (Å)	10.721(2)	10.7071(4)	11.1467(2)	10.708(2)
c (Å)	10.339(2)	10.3296(4)	10.6165(2)	10.439(2)
β (°)	118.05(3)	117.7800(10)	118.2090(10)	117.772(3)
V(Å^3)	1367.2(6)	1381.38(9)	1518.22(5)	1388.6(5)
$Z/D_{calc.}$ (g cm^{-3})	2/1.579	2/1.990	2/2.222	2/1.767
μ (mm^{-1})	1.222	6.609	4.817	3.889
F(000)	662	806	950	734
θ range (°)	2.517–26.166	2.506–33.326	2.420–42.233	2.793–26.980
h; k; l ranges	±17; ±13; ±12	±21; ±16; ±15	±27; −20, 21; −19, 20	±17; ±13, ±13
Reflections collected	9194	25 601	39 452	21 440
Independent reflect. (R_{int})	2699 (0.0577)	5317 (0.0393)	10 671 (0.0269)	3009 (0.0268)
Data completeness (%)	99.9	99.8	99.9	99.6
Data/restraints/parameters	2699/1/178	5317/1/179	10 671/1/178	3009/1/179
Goodness-of-fit on F^2 [a]	1.018	1.041	1.063	1.057
R_1/wR_2 [$I > 2\sigma(I)$][b]	0.0403/0.0980	0.0237/0.0473	0.0329/0.0801	0.0193/0.0474
R_1/wR_2 (all data)[b]	0.0426/0.0991	0.0290/0.0491	0.0418/0.0844	0.0207/0.0483
Max./min. $\Delta\rho$ (e Å^{-3})[c]	0.496/−0.799	0.616/−0.508	1.915/−0.827	0.405/−0.212
Flack parameter[d]	0.06(2)	0.025(8)	0.022(18)	0.032(9)
CCDC number	1943411	1943413	1943414	1943412

[a] Goodness-of-fit = $[\sum[w(F_o^2 - F_c^2)^2]/(n-p)]^{1/2}$. [b] $R_1 = [\sum(||F_o| - |F_c||)/\sum|F_o|]$; w$R_2 = [\sum[w(F_o^2 - F_c^2)^2]/\sum[w(F_o^2)^2]]^{1/2}$. [c] Largest difference peak and hole. [d] Absolute structure parameter.

Table 10 Crystal data and structures refinement details

	Λ-Cu-*S*1 (#1)	Λ-Cu-*S*1 (#2)	Δ-Cu-*S*2	Δ-Cu-*S*3	Δ-Cu-*S*4
Data set	*S*-Cl2 + Cu	*S*-Cl2 + Cu + Bruno	*S*-Br2 + Cu	*S*-I2 + Cu	*S*-ClBr + Cu
Empirical formula	$C_{30}H_{24}Cl_4CuN_2O_2$	$C_{30}H_{24}Cl_4CuN_2O_2$	$C_{30}H_{24}Br_4CuN_2O_2$	$C_{30}H_{24}I_4CuN_2O_2$	$C_{30}H_{24}Br_2Cl_2CuN_2O_2$
M (g mol^{-1})	649.85	649.85	827.69	1015.65	738.77
Temperature (K)	140.01(10)	273(2)	293(2)	296(2)	140.00(10)
Wavelength (Å)	1.54184	0.71073	0.71073	0.71073	1.54184
Crystal system	Monoclinic	Monoclinic	Monoclinic	Monoclinic	Monoclinic
Space group	$P2_1$	$P2_1$	$I2$	$C2$	$I2$
a (Å)	8.57142(6)	8.6322(2)	10.427(2)	14.5549(3)	10.33616(17)
b (Å)	14.70541(11)	14.8439(3)	10.778(2)	11.1475(3)	10.64041(15)
c (Å)	11.09232(8)	11.1572(3)	13.058(3)	10.6074(3)	13.0212(2)
β (°)	97.2834(7)	97.8710(10)	106.74(3)	118.1800(10)	107.5551(17)
V (Å^3)	1386.863(18)	1416.16(6)	1405.3(5)	1517.06(7)	1365.39(4)
$Z/D_{calc.}$ (g cm^{-3})	2/1.556	2/1.524	2/1.956	2/2.223	2/1.797
μ (mm^{-1})	4.917	1.180	6.496	4.820	6.623
F(000)	662	662	806	950	734
θ range (°)	4.018–76.011	2.297–32.581	2.495–26.996	2.178–34.717	4.815–76.200
h; k; l ranges	−8, 10; −14, 18; ±13	±13; ±22; ±16	±13; ±13; ±16	±23; ±17; ±16	±12; ±13; −16, 10
Reflections collected	9280	79 451	14 689	31 030	4427
Independent reflect. (R_{int})	4988 (0.0143)	10 276 (0.0669)	3060 (0.0263)	6381 (0.1195)	2606 (0.0143)
Data completeness (%)	100.0	100.0	99.7	100.0	100.0
Data/restraints/parameters	4988/1/355	10 276/1/352	3060/1/177	6381/1/177	2606/1/178
Goodness-of-fit on F^2 [a]	1.043	0.993	1.038	1.054	1.060
R_1/wR_2 [$I > 2\sigma(I)$][b]	0.0251/0.0655	0.0288/0.0659	0.0185/0.0425	0.0452/0.1132	0.0247/0.0654
R_1/wR_2 (all data)[b]	0.0251/0.0655	0.0378/0.0729	0.0207/0.0430	0.0506/0.1179	0.0248/0.0654
Max./min. $\Delta\rho$ (e Å^{-3})[c]	0.316/−0.377	0.594/−0.352	0.459/−0.198	3.719/−1.722	0.580/−0.471
Flack parameter[d]	0.010(11)	−0.005(4)	0.023(4)	0.021(14)	−0.03(2)
CCDC number	1943418	1964878	1943419	1943420	1943417

[a] Goodness-of-fit = $[\sum[w(F_o^2 - F_c^2)^2]/(n-p)]^{1/2}$. [b] $R_1 = [\sum(||F_o| - |F_c||)/\sum|F_o|]$; w$R_2 = [\sum[w(F_o^2 - F_c^2)^2]/\sum[w(F_o^2)^2]]^{1/2}$. [c] Largest difference peak and hole. [d] Absolute structure parameter.

b3lyp, m06) and the basis sets (tzvp, svp and sdd) on the optimized structures. The best fit to the experimental spectra was obtained at m06/tzvp//b3lyp/6-31g(d) level of theory. UV-Vis. and ECD spectral patterns, obtained from different combinations of the functionals and the basis sets, are almost identical with little shifted bands maxima (λ_{max}), strongly support the reliability and validity of the methods used (Fig. S8, ESI†). The PCM (polarization continuum model) was incorporated using chloroform as solvent and 72 excited states (roots) were considered for calculations (Table S1†). The simulated spectra (UV-Vis. and ECD) were generated using the program SpecDis[41] by applying Gaussian band shape with exponential half-width σ = 0.33 eV. Finally, assignments on the simulated spectra and molecular orbitals (HOMOs and LUMOs) were made at the same level of theory.

Conflicts of interest

There are no conflicts of interest to declare.

Acknowledgements

The authors are grateful to the Research Council of the University of Isfahan (Iran) for financial support of this work. We acknowledge Wazed Miah Science Research Centre (WMSRC) and Department of Chemistry, Jahangirnagar University, Bangladesh for obtaining UV-Vis., and DSC data. Our Sincere thanks to Professor Walid Houry and Vaibhav Bhandari, Department of Biochemistry, Faculty of Medicine, University of Toronto, for obtaining ECD spectra. We thank to Professor ABP Lever, Department of Chemistry, York University, Toronto and the computecanada.ca (https://ccdb.computecanada.ca/) Ontario, Canada for using computational resources. I. Correia thanks the financial support from Fundação para a Ciência e Tecnologia (FCT), through project UIDB/00100/2020 and the program Investigador FCT.

Notes and references

1 (*a*) A. von Zelewsky, *Stereochemistry of Coordination Compounds*, John Wiley & Sons, Chichester, 1996, p. 69; (*b*) H. Amouri and M. Gruselle, *Chirality in Transition Metal Chemistry: Molecules, supramolecular assemblies and materials*, John Wiley & Sons, Chichester, 2008, p. 40; (*c*) E. C. Constable, *Chem. Soc. Rev.*, 2013, **42**, 1637; (*d*) K. A. Jensen, *Inorg. Chem.*, 1970, **9**, 1; (*e*) U. Knof and A. von Zelewsky, *Angew. Chem., Int. Ed.*, 1999, **38**, 302; (*f*) O. Mamula, A. von Zelewsky, T. Bark, H. Stoeckli-Evans, A. Neels and G. Bernardinelli, *Chem. – Eur. J.*, 2000, **6**, 3575.

2 (*a*) C. Evans and D. Luneau, *J. Chem. Soc., Dalton Trans.*, 2002, 83; (*b*) R. E. Ernst, M. J. O'Connor and R. H. Holm, *J. Am. Chem. Soc.*, 1967, **89**, 6104; (*c*) G. Brewer, C. Brewer,

 This journal is © The Royal Society of Chemistry 2020

R. J. Butcher, G. T. Robichaux and C. Viragh, *Inorg. Chim. Acta*, 2014, **410**, 171.
3 (*a*) E. C. Constable, G. Zhang, C. E. Housecroft, M. Neuburger and J. A. Zampese, *Chem. Commun.*, 2010, 3077; (*b*) F. Wang, H. Zhang, L. Li, H.-Q. Hao, X.-Y. Wang and J.-G. Chen, *Tetrahedron: Asymmetry*, 2006, **17**, 2059; (*c*) T. Ohno, S. Chorazy, K. Imoto and S. Ohkoshi, *Cryst. Growth Des.*, 2016, **16**, 4119.
4 (*a*) H. Sakiyama, H. Okawa, N. Matsumoto and S. Kida, *Bull. Chem. Soc. Jpn.*, 1991, **64**, 2644; (*b*) H. Sakiyama, H. Okawa, N. Matsumoto and S. Kida, *J. Chem. Soc., Dalton Trans.*, 1990, 2935; (*c*) Z. Dezhahang, M. R. Poopari, J. Cheramy and Y. J. Xu, *Inorg. Chem.*, 2015, **54**, 4539.
5 (*a*) H. Ōkawa, M. Nakamura and S. Kida, *Inorg. Chim. Acta*, 1986, **120**, 185; (*b*) T. Akitsu and Y. Einaga, *Polyhedron*, 2005, **24**, 2933; (*c*) T. Akitsu and Y. Einaga, *Polyhedron*, 2005, **24**, 1869; (*d*) T. Akitsu and Y. Einaga, *Acta Crystallogr., Sect. C: Cryst. Struct. Commun.*, 2004, **60**, m640; (*e*) T. Akitsu, *Polyhedron*, 2007, **26**, 2527.
6 (*a*) C. Gan, G. Lai, Z. Zhang, Z. Wang and M.-M. Zhou, *Tetrahedron: Asymmetry*, 2006, **17**, 725; (*b*) M. Itagaki, K. Hagiya, M. Kamitamari, K. Masumoto, K. Suenobu and Y. Yamamoto, *Tetrahedron*, 2004, **60**, 7835; (*c*) Z. Li, G. Liu, Z. Zheng and H. Chen, *Tetrahedron*, 2000, **56**, 7187; (*d*) A. Zulauf, M. Mellah, X. Hong and E. Schulz, *Dalton Trans.*, 2010, **39**, 6911; (*e*) K. Matsumoto, B. Saito and T. Katsuki, *Chem. Commun.*, 2007, 3619.
7 (*a*) K. C. Gupta and A. K. Sutar, *Coord. Chem. Rev.*, 2008, **252**, 1420; (*b*) I. Karamé, M. Jahjah, A. Messaoudi, M. L. Tommasino and M. Lemaire, *Tetrahedron: Asymmetry*, 2004, **15**, 1569; (*c*) I. Karamé, M. L. Tommasino, R. Faure and M. Lemaire, *Eur. J. Org. Chem.*, 2003, 1271; (*d*) Z.-H. Yang, L.-X. Wang, Z.-H. Zhou, Q.-L. Zhou and C.-C. Tang, *Tetrahedron: Asymmetry*, 2001, **12**, 1579; (*e*) P. Guo and K.-Y. Wong, *Electrochem. Commun.*, 1999, **1**, 559; (*f*) A. L. Iglesias, G. Aguirre, R. Somanathan and M. Parra-Hake, *Polyhedron*, 2004, **23**, 3051.
8 G. Pescitelli, S. Lüdeke, A.-C. Chamayou, M. Marolt, V. Justus, M. Górecki, L. Arrico, L. Di Bari, M. A. Islam, I. Gruber, M. Enamullah and C. Janiak, *Inorg. Chem.*, 2018, **57**, 13397.
9 M. Enamullah, A. K. M. Royhan Uddin, G. Pescitelli, R. Berardozzi, G. Makhloufi, V. Vasylyeva, A.-C. Chamayou and C. Janiak, *Dalton Trans.*, 2014, **43**, 3313.
10 M. Enamullah, G. Makhloufi, R. Ahmed, B. Alif Joy, M. A. Islam, D. Padula, H. Hunter, G. Pescitelli and C. Janiak, *Inorg. Chem.*, 2016, **55**, 6449.
11 A.-C. Chamayou, G. Makhloufi, L. A. Nafie, C. Janiak and S. Lüdeke, *Inorg. Chem.*, 2015, **54**, 2193.
12 A.-C. Chamayou, S. Lüdeke, V. Brecht, T. B. Freedman, L. A. Nafie and C. Janiak, *Inorg. Chem.*, 2011, **50**, 11363.
13 M. Enamullah, M. A. Quddus, M. R. Hasan, G. Pescitelli, R. Berardozzi, G. J. Reiß and C. Janiak, *Eur. J. Inorg. Chem.*, 2015, 2758.
14 M. Enamullah, V. Vasylyeva and C. Janiak, *Inorg. Chim. Acta*, 2013, **408**, 109.
15 C. Merten, R. McDonald and Y. Xu, *Inorg. Chem.*, 2014, **53**, 3177.
16 (*a*) M. Albrecht, E. Isaak, M. Baumert, V. Gossen, G. Raabe and R. Fröhlich, *Angew. Chem., Int. Ed.*, 2011, **50**, 2850; (*b*) C. M. álvarez, R. Carrillo, R. García-Rodríguez and D. Miguel, *Chem. Commun.*, 2011, **47**, 12765.
17 (*a*) J. Gregoliński, M. Hikita, T. Sakamoto, H. Sugimoto, H. Tsukube and H. Miyake, *Inorg. Chem.*, 2016, **55**, 633; (*b*) S. Zahn and J. W. Canary, *Science*, 2000, **288**, 1404.
18 M. Enamullah, M. A. Quddus, M. R. Hasan, G. Pescitelli, R. Berardozzi, G. Makhloufi, V. Vasylyeva and C. Janiak, *Dalton Trans.*, 2016, **45**, 667.
19 M. Enamullah, A. K. M. Royhan, A.-C. Chamayou and C. Janiak, *Z. Naturforsch., B: Chem. Sci.*, 2007, **62**, 807.
20 (*a*) W. J. Geary, *Coord. Chem. Rev.*, 1971, **7**, 81; (*b*) I. Kuzniarska-Biernacka, K. Kurzak, B. Kurzak and J. Jezierska, *J. Solution Chem.*, 2003, **32**, 719.
21 (*a*) H. D. Flack, M. Sadki, A. L. Thompson and D. J. Watkin, *Acta Crystallogr., Sect. A: Fundam. Crystallogr.*, 2011, **67**, 21; (*b*) H. D. Flack and G. Bernardinelli, *Chirality*, 2008, **20**, 681; (*c*) H. D. Flack and G. Bernardinelli, *Acta Crystallogr., Sect. A: Fundam. Crystallogr.*, 1999, **55**, 908; (*d*) H. Flack, *Acta Crystallogr., Sect. A: Fundam. Crystallogr.*, 1983, **39**, 876.
22 Y. Shibuya, K. Nabari, M. Kondo, S. Yasue, K. Maeda, F. Uchida and H. Kawaguchi, *Chem. Lett.*, 2008, **37**, 78.
23 L. Yang, D. R. Powell and R. P. Houser, *Dalton Trans.*, 2007, 955.
24 M. J. Turner, J. J. McKinnon, S. K. Wolff, D. J. Grimwood, P. R. Spackman, D. Jayatilaka and M. A. Spackman, *CrystalExplorer 17*, University of Western Australia, 2017. http://hirshfeldsurface.net.
25 (*a*) G. Cavallo, P. Metrangolo, R. Milani, T. Pilati, A. Priimagi, G. Resnati and G. Terraneo, *Chem. Rev.*, 2016, **116**, 2478; (*b*) P. Metrangolo and G. Resnati, *Halogen Bonding. Fundamentals and Applications*, Springer-Verlag, Berlin, Heidelberg, 2008; (*c*) M. Aryaeifar, H. A. Rudbari and G. Bruno, *Polyhedron*, 2018, **155**, 114.
26 P. Politzer, J. S. Murray and T. Clark, *Phys. Chem. Chem. Phys.*, 2013, **15**, 11178.
27 (*a*) A. Mukherjee, S. Tothadi and G. R. Desiraju, *Acc. Chem. Res.*, 2014, **47**, 2514; (*b*) S. K. Nayak, M. K. Reddy, T. N. G. Row and D. Chopra, *Cryst. Growth Des.*, 2011, **11**, 1578; (*c*) O. V. Shishkin, *Chem. Phys. Lett.*, 2008, **458**, 96.
28 (*a*) M. Enamullah and M. K. Islam, *J. Coord. Chem.*, 2013, **66**, 4107; (*b*) M. Enamullah, M. A. Quddus, M. M. Rahman and T. E. Burrow, *J. Mol. Struct.*, 2017, **1130**, 765; (*c*) I. Veroni, A. Rontoyianni and C. A. Mitsopoulou, *Dalton Trans.*, 2003, 255; (*d*) https://people.chem.umass.edu/xray/solvent.html.
29 (*a*) P.-K. Chow, G. Cheng, G. S. M. Tong, C. Ma, W.-M. Kwok, W.-H. Ang, C. Y.-S. Chung, C. Yang, F. Wang and C.-M. Che, *Chem. Sci.*, 2016, **7**, 6083; (*b*) W. Lu, B.-X. Mi, M. C. W. Chan, Z. Hui, C.-M. Che, N. Zhu and S.-T. Lee, *J. Am. Chem. Soc.*, 2004, **126**, 4958; (*c*) J. A. G. Williams, *Top. Curr. Chem.*, 2007, **281**, 205.
30 (*a*) A. G. Martynov, J. Mack, A. K. May, T. Nyokong, Y. G. Gbunova and A. Y. Tsivadze, *ACS Omega*, 2019, **4**,

7265; (*b*) C. Bannwarth and S. Grimme, *Comput. Theor. Chem.*, 2014, **45**, 1040; (*c*) S. Grimme, *J. Chem. Phys.*, 2013, **138**, 244104; (*d*) C. Bannwarth, J. Seibert and S. Grimme, *Chirality*, 2016, **28**, 365; (*e*) T. Risthaus, A. Hansen and S. Grimme, *Phys. Chem. Chem. Phys.*, 2014, **16**, 14408; (*f*) A. Vacher, A. Amar, F. Camerel, Y. Molard, C. Latouche, T. Roisnel, V. Dorcet, A. Boucekkine, H. Akdas-Kiliç and M. Achard, *Dalton Trans.*, 2019, **48**, 2128.

31 (*a*) A. Rockenbauer and L. Korecz, *Appl. Magn. Reson.*, 1996, **10**, 29; (*b*) U. Sakaguchi and A. W. Addison, *J. Chem. Soc., Dalton Trans.*, 1979, 600.

32 *CrysAlisPro, Rigaku Oxford Diffraction, release 1.171.39.46*, 2018.

33 A. J. Duisenberg, L. M. Kroon-Batenburg and A. M. Schreurs, *J. Appl. Crystallogr.*, 2003, **36**, 220.

34 R. H. Blessing, *Acta Crystallogr., Sect. A: Found. Crystallogr.*, 1995, **51**, 33.

35 (*a*) *COSMO, version 1.60*, Bruker AXS Inc., Madison, Wisconsin, 2005; (*b*) *SAINT, version 7.06A*, Bruker AXS Inc., Madison, Wisconsin, 2005; (*c*) *SADABS, version 2.10*, Bruker AXS Inc., Madison, Wisconsin, 2005.

36 G. M. Sheldrick, *SHELXT* - Integrated space-group and crystal-structure determination, *Acta Crystallogr., Sect. A: Found. Adv.*, 2015, **71**, 3.

37 G. M. Sheldrick, *SHELXL* - Crystal structure refinement, *Acta Crystallogr., Sect. C: Struct. Chem.*, 2015, **71**, 3.

38 Bruker-AXS, *APEX3 v2016.1-0*, Madison, Wisconsin, USA, 2016.

39 G. M. Sheldrick, A short history of *SHELX*, *Acta Crystallogr., Sect. A: Found. Crystallogr.*, 2008, **64**, 112.

40 M. J. Frisch, G. W. Trucks, H. B. Schlegel, G. E. Scuseria, M. A. Robb, J. R. Cheeseman, G. Scalmani, V. Barone, B. Mennucci, G. A. Petersson, H. Nakatsuji, M. Caricato, X. Li, H. P. Hratchian, A. F. Izmaylov, J. Bloino, G. Zheng, J. L. Sonnenberg, M. Hada, M. Ehara, K. Toyota, R. Fukuda, J. Hasegawa, M. Ishida, T. Nakajima, Y. Honda, O. Kitao, H. Nakai, T. Vreven, J. A. Montgomery Jr., J. E. Peralta, F. Ogliaro, M. Bearpark, J. J. Heyd, E. Brothers, K. N. Kudin, V. N. Staroverov, R. Kobayashi, J. Normand, K. Raghavachari, A. Rendell, J. C. Burant, S. S. Iyengar, J. Tomasi, M. Cossi, N. Rega, J. M. Millam, M. Klene, J. E. Knox, J. B. Cross, V. Bakken, C. Adamo, J. Jaramillo, R. Gomperts, R. E. Stratmann, O. Yazyev, A. J. Austin, R. Cammi, C. Pomelli, J. W. Ochterski, R. L. Martin, K. Morokuma, V. G. Zakrzewski, G. A. Voth, P. Salvador, J. J. Dannenberg, S. Dapprich, A. D. Daniels, Ö. Farkas, J. B. Foresman, J. V. Ortiz, J. Cioslowski and D. J. Fox, *Gaussian 09, Revision D.01*, Gaussian, Inc., Wallingford CT, 2009.

41 T. Bruhn, A. Schaumlöffel, Y. Hemberger and G. Bringmann, *Chirality*, 2013, **25**, 243.

 This journal is © The Royal Society of Chemistry 2020